Label2label: Training a neural network to selectively restore cellular structures in fluorescence microscopy

Lisa Sophie Kölln[1-3,*], Omar Salem[2,3], Jessica Valli[4], Carsten Gram Hansen[2,3,†], Gail McConnell[1,†]

[1] University of Strathclyde, Department of Physics, Glasgow, UK

[2] University of Edinburgh, Centre for Inflammation Research, Edinburgh, UK

[3] University of Edinburgh, Institute for Regeneration and Repair, Edinburgh, UK

[4] Edinburgh Super Resolution Imaging Consortium, Institute of Biological Chemistry, Biophysics and Bioengineering, Heriot-Watt University, Edinburgh, UK

[*] corresponding author: lisa.kolln@strath.ac.uk

[†] last author

Key words: image content filter, fluorescence microscopy, antibody labelling, deep learning, convolutional neural networks, content-aware image restoration, noise2noise, cellular structures, focal adhesions, actin cytoskeleton, microtubule network, caveolae

Abstract

Fluorescence microscopy is an essential tool in cell biology to visualise the spatial distribution of proteins that dictates their role in cellular homeostasis, dynamic cellular processes, and dysfunction during disease. However, unspecific binding of the antibodies that are used to label a cellular target often leads to high background signals in the images, decreasing the contrast of a cellular structure of interest. Recently, convolutional neural networks (CNNs) have been successfully employed for denoising and upsampling in fluorescence microscopy, but current image restoration methods cannot correct for background signals originating from the label. Here, we report a new method to train a CNN as content filter for non-specific signals in fluorescence images that does not require a clean benchmark, using dual-labelling to generate the training data. We name this method *label2label* (L2L). In L2L, a CNN is trained with image pairs of two non-identical labels that target the same cellular structure of interest. We show that after L2L training a network restores images not only with reduced image noise but also label-induced unspecific fluorescence signal in images of a variety of cellular structures, resulting in images with enhanced structural contrast. By implementing a multi-scale structural similarity loss function, the performance of the CNN as a content filter is further enhanced, for example, in STED images of caveolae. We show evidence that, for this loss function, sample differences in the training data significantly decrease so-called hallucination effects in the restorations that we otherwise observe when training the CNN with images of the same label. We also assess the

performance of a cycle generative adversarial network as a content filter after L2L training with unpaired image data. Lastly, we show that a CNN can be trained to separate structures in superposed fluorescence images of two different cellular targets, allowing multiplex imaging with microscopy setups where the number of excitation sources or detectors is limited.

Introduction

In recent years, deep learning has increasingly been used for image processing in cell biology [1]. Specifically, convolutional neural networks (CNNs) with, or closely related to, a U-Net architecture [2] are employed for various tasks, from protein detection in transmission microscopy images [3], [4], to image segmentation of single cells [5] or cellular structures such as the nucleus [6]. CNNs have also been used in medical applications, for example, for cell density estimation in corneal endothelial specular microscopy images [7] or tumour classification of urothelial cell carcinoma in pathology [8].

Fluorescence microscopy is a commonly used technique in cell biology to determine the spatial distribution and abundance of target proteins in cells. It relies on the use of highly specific labels to visualise the cellular components of interest. Fluorescent labels can be chemical stains, antibody (AB) labelling or molecular labelling, where cells are genetically altered to express fluorescent proteins [9]. Here, we mainly focus on immunofluorescence (IF) labelling in fixed cells.

Recently, CNNs were employed for content-aware image restoration (CARE) of corrupted fluorescence images. By training a U-Net with image pairs that were generated at different laser powers, or different exposure times, respectively, it was shown that a trained network was able to successfully restore denoised images of cell structures like the cell membrane and the nucleus [2], [10]. The CNN could further be utilised to up-sample images that were detected below the Nyquist sampling frequency [10]. Moreover, generative adversarial networks (GAN) were trained to enhance image resolution in IF microscopy images, using total internal reflection microscopy (TIRF) or stimulated emission depletion (STED) microscopy to acquire the training benchmarks [11], [12].

Both mentioned methods rely on clean benchmark images for the network training which are challenging to acquire in practice. Hence, semi-/unsupervised deep learning-based restoration methods have emerged in IF microscopy. For instance, networks based on the architecture of a cycle generative adversarial network (cycleGAN) [13] were employed to deconvolve fluorescence images of microtubules, using unpaired higher resolution images as reference [14] or simulated low- and high-resolution images [15] for the training. CycleGANs allow the training with unaligned image pairs, addressing the “hallucination problem”, - the introduction of artificial features in the generated images, - when training a classical GAN with unpaired data by implementing an additional training

instance in which a second GAN is trained to translate the generated, fake image back to the input [13], [15]. Other examples include *noise2void*, an unsupervised method to remove camera shot noise [16], *DivNoising*, which is based on a variational autoencoder that is trained to restore a distribution of denoised images based on a noise model [17], and *noise2noise* (N2N) [18]. For N2N, a neural network is trained with corrupted image pairs of the same sample. Here, due to the statistical nature of how loss is minimised by the network during training with a deviation-minimising loss function, it was shown that uncorrelated image signals like Gaussian, Poisson or Bernoulli noise are rejected while correlating fluorescence signal is recovered by a network (see 'Loss Functions for Training a CNN') [18].

While these image restoration methods enhance the contrast in IF images by upsampling or denoising, all mentioned methods do not correct for inherent background signals in the specimen itself which, in IF microscopy, originate from the cell label or labelling protocol. Unspecific labelling by a stain or antibody binding, as well as internalisation or residue dyes after the specimen preparation, can significantly limit the image contrast of a cell component of interest [19]. The performance of antibodies or stains can vary for different reasons. For instance, epitopes-can be altered in the target protein by the fixation step, effectively changing the location or accessibility to the antibody [20]. Also, unspecific antibody binding can be caused by attractive intermolecular interaction such as van der Waals or hydrogen bonding interactions, or by binding to proteins with similar epitopes, which overall results in an underlying cytosolic background signal in images of cells [21].

Label2label

We propose a new application of deep learning in fluorescence microscopy where a neural network is trained as a content filter of label-induced unspecific cytosolic signals in fluorescence images of distinct cellular structures. We call this method *label2label* (L2L). For L2L, a CNN is trained with image pairs of cells that were dual-labelled for the same distinct cellular structure of interest. L2L utilises the varying performance of antibodies and stains in fluorescence microscopy. We hypothesized that a CNN trained with two images of a cellular structure that originate from two non-identical labels and therefore exhibit sample differences would act as a content filter - where fluorescence signals that systematically vary in the images are rejected, while correlating, cellular structures are restored. Therefore, L2L is different to N2N. In both methods a network is trained without clean benchmark images, but in L2L differences between the training input and benchmark images are not only originating from dynamic image corruptions like noise, but also inherent sample (=label) differences. Consequently, undesired signals originating from cytosolic protein and unspecific binding are retrieved in restorations after N2N training, whereas with L2L we show that a network can be trained as filter for such image content after strategic selection of the training data.

97 L2L is also different to restoration methods with a *noise2clean* approach such as CARE, where a CNN
98 is trained with images of the same label that were taken under different imaging conditions [10]. While
99 image pairs for *noise2clean* training can be generated with one microscope by, for example, varying
100 exposure time, frame averaging or the sampling density, this approach is rarely necessary in IF
101 microscopy where cell specimens are non-dynamic and exhibit comparably high photon counts. Here,
102 generating the necessary image pairs for the network training is time-consuming and significantly
103 complicated by stage drift resulting in a low benefit-cost ratio. More importantly, as in N2N,
104 background signals originating from the label are still present in the training benchmark, and as such
105 they cannot be corrected by this method.

106 For L2L training, the images for the training are acquired mostly simultaneously of dual-labelled cells,
107 under near-identical imaging conditions (see 'Methods: Imaging'). The images obtained using one
108 fluorescent cell label are selected as training input, while the images from the label that yield a higher
109 contrast of the cellular structure are used as training benchmark. We selected the CSBDeep framework
110 for the training that was previously used for CARE of noisy or under-sampled fluorescence images [10].
111 Moreover, for one dataset, we trained a cycleGAN with unpaired images of the two labels to assess if,
112 in principle, a network can also be trained as content filter using IF images that stem from two
113 separately prepared and imaged cell specimens for the training [13].

114 To establish and evaluate how our method performs we generated image data for L2L training across
115 four different distinct cellular structures: the actin cytoskeleton, the microtubule network, caveolae
116 and focal adhesions. Actin is a conserved protein in eukaryotic cells that plays a major role in cellular
117 functions like cell migration, cell motility or sustaining the cell shape [22], [23]. Actin exists in two
118 states: as globular (G-) actin in its monomeric form, or polymerised as filamentous (F-) actin [24]. There
119 is evidence that different actin isomers vary in function and localisation; they can appear, for example,
120 in stress fibres, circular bundles, cell-cell contacts or the cell cortex [25]. Microtubules are
121 fundamental cytoskeletal polymeric structures in all eukaryotic cells that, amongst others, play a part
122 in cell transport, cellular signalling via cilia and cell division [26]. The inhibition as well as the promotion
123 of microtubule assembly has been shown to promote mitotic arrest which makes microtubules a
124 prominent target in cancer therapy research [27]. Caveolae are 60-100 nm plasma membrane
125 invaginations composed of heterooligomeric CAVEOLIN and CAVIN protein complexes and abundant
126 in many mammalian cell types [28], [29]. Caveolae are multifunctional organelles that are implicated
127 in transcytosis, lipid homeostasis and cellular signalling. Both CAVEOLIN1 and CAVIN1 are essential for
128 caveolae formation in non-muscle cells [30]. Focal adhesions (FAs) are cellular membrane-associated
129 multi-protein component biomechanical structures. FAs are integral in the ability for most cells to
130 sense and respond to the extracellular matrix and physical changes in the cellular microenvironment,

FAs thereby function as central cellular contact points with the extracellular environment, that relay and transmit dynamic external information as internal cellular signalling events [30], [31].

The ability of a CNN to distinguish cellular structures in fluorescence images that was observable in the qualitative results after L2L training in this work was further assessed by training a CNN to separate a nuclear and a plasma membrane marker in superposed IF images of cells that were labelled with a nuclear marker and an antibody against the plasma membrane protein CD44 (see last results section).

Loss functions for training a convolutional neural network

We used different loss functions to train a CNN with the aim to restore cell images with enhanced structural contrast. A CNN, which can be described as a function g_ϑ with all its model parameters ϑ, is trained to minimise the error between two images based on a loss function L:

$$\underset{\vartheta}{\operatorname{argmin}} \sum_{t=1}^{T} L(g_\vartheta(x_t), y_t) \,, \qquad [1]$$

with $g_\vartheta(x_t)$ as the predicted image for the input x_t, y_t as the benchmark and T as the number of input-benchmark image pairs that are used for the training [18].

The most commonly used deviation-minimising estimators are the least absolute deviation loss function L_1 (or *LAD*) and the least square deviation loss function L_2 (or *LSD*) [18], [32]:

$$L_1(\hat{x}_t, y_t) = \frac{1}{N} \sum_{n=1}^{N} \left| \hat{y}_{t,n} - y_{t,n} \right| \,, \qquad [2]$$

$$L_2(\hat{x}_t, y_t) = \frac{1}{N} \sum_{n=1}^{N} \left(\hat{y}_{t,n} - y_{t,n} \right)^2 \,, \qquad [3]$$

where $\hat{y}_t$ (=$g_\vartheta(x_t)$) is the predicted image and N is the number of pixels in the image.

Since L_2 is minimal if it equals the mean value of the observations, it was previously used for N2N training in cases where the image corruption is, for example, Gaussian noise that, on average, is zero [18]. L_1 is the loss function of the CSBDeep framework in default configuration (for non-probabilistic training). With both, L_1 and L_2, the network calculates the average loss on a pixel-to-pixel basis which limits the ability of the network to consider 2-dimensional correlating signal of structures in an image. As a result, predicted images from a CNN trained with L_1 or L_2 are often of low quality for a human observer [32], [33].

A multi-scale structural similarity (*MS-SSIM*) index was proposed to compare structural signal between two images that takes the properties of the human visual system into account [34], [35]. The *M*-scale *SSIM* index for a pixel *p* is calculated as follows, after making assumptions as outlined in [35]:

$$MS - SSIM(p) = (l_M(p))^{\gamma_M} \cdot \prod_{j=1}^{M} (c_j(p))^{\gamma_j} \cdot (s_j(p))^{\gamma_j} \,, \qquad [4]$$

with the exponent γ_j as the weight for the individual scale j ($\sum_{j=1}^{M} \gamma_j = 1$), and measures that compare the luminance (l_M), the contrast (c_j) and structure (s_j) of two images. These measures are functions of the local statistics: the sample mean $\mu_{\hat{y}_p/y_p}$, the sample variance $\sigma^2_{\hat{y}_p/y_p}$ and the sample correlation coefficient $\sigma^2_{\hat{y}_p y_p}$ between two image patches $\hat{y}_p$ and y_p that are the local neighbourhood of a centre pixel p [34]. They are described as:

$$l(\hat{x}_p, y_p) = \frac{2\mu_{\hat{y}_p}\mu_{y_p} + (K_1R)^2}{\mu^2_{\hat{y}_p} + \mu^2_{y_p} + (K_1R)^2}, \; c(\hat{x}_p, y_p) = \frac{2\sigma_{\hat{y}_p}\sigma_{y_p} + (K_2R)^2}{\sigma^2_{\hat{y}_p} + \sigma^2_{y_p} + (K_2R)^2}, \; s(\hat{x}_p, y_p) = \frac{2\sigma_{\hat{y}_p y_p} + (K_2R)^2}{2\sigma_{\hat{y}_p}\sigma_{y_p} + (K_2R)^2}. \quad [5\text{-}7]$$

Here, K_1 and K_2 are small constants, R is the dynamic range of the image and a Gaussian weighting function is used to calculate the local statistics of a pixel in the two images (as in [34]). To calculate the *MS-SSIM* index for $M > 1$, a low-pass filter is applied to the image patches after each iteration, followed by down-sampling by a factor of 2. This approach makes the MS-SSIM index sensitive to differing viewing conditions, such as differing perceived resolution from the point of observation. In [35], the weights γ_j were experimentally determined as (0.0448, 0.2856, 0.3001, 0.2363, 0.1333) to calculate the *5S-SSIM* index (M=5) for a representative image example.

The *MS-SSIM* index exhibits values between (-1, 1) where 0 implies no structural similarity and -1/1 a negative/positive correlation between two images. Since a network aims at minimising loss during training, for a multi-scale SSIM loss function ($L_{MS\text{-}SSIM}$) follows [32]:

$$L_{MS-SSIM}(\hat{y}_t, y_t) = 1 - \frac{1}{N}\sum_{n=1}^{N} MS - SSIM(\hat{y}_{t,n}, y_{t,n}). \quad [8]$$

We hypothesized that a CNN would restore images with higher structural contrast after L2L training with a MS-SSIM loss function compared to when using a "classical" L_1. To test this hypothesis, we trained a CNN using a L_1, L_{SSIM} (M=1), $L_{3S\text{-}SSIM}$ (M=3) and a $L_{5S\text{-}SSIM}$ (M=5), respectively. The results of the trainings were compared to the denoising method N2N. For N2N training, the same pre-processing steps and network settings were applied, but two noise realisations of the same label were used as training input and benchmark instead that were acquired through sequential imaging. We wondered if using a $L_{MS\text{-}SSIM}$ instead of a L_1 for N2N training, would train a CNN to restore images not only with reduced image noise but also increased contrast of the cellular structure. The aim of this work is to compare two deep learning-based restoration methods that improve the contrast of cellular structures in fluorescence images, do not require clean benchmark data and whose requirements for the training data generation are feasible in standard IF microscopy. We show that by introducing systematic sample differences in the training data a CNN can be successfully trained to reject not only image noise but also diffuse cytosolic signals in IF images that are label-dependent and, in practice, decrease the image contrast of a target structure.

185 # Results

186 ## Label2label to filter out de-polymerised β-actin in images of HeLa cells

187 To study the performance of a CNN after L2L training with images of the actin cytoskeleton, image
188 pairs of HeLa cells (*N*=68) were generated that were fixed 6 hours after plating, and dual-labelled with
189 the monoclonal anti-β-actin antibody AC-15 and a phalloidin stain (see 'Methods: Sample preparation
190 for IF microscopy' and 'Methods: Imaging'). **Figure 1A** shows an example confocal image pair of the
191 fixed cell specimen. While the phalloidin stain labels almost exclusively the actin filaments, images of
192 the monoclonal anti-β-actin exhibit a high underlying fluorescence signal in the cell body, likely caused
193 by unspecific binding and/or binding to cytosolic protein that result in high intensity punctate regions
194 in the cytoplasm. Notably, a "cleaner", 20-frame average image of AC-15 exhibits less image noise,
195 but non-filamentous background signal is still present throughout the cell body (see **Figure 1C**). The
196 difference in image contrast between both labels is quantifiable by calculating the mean Michelson
197 and RMS contrast for the images of each label (see [36]). To calculate these, we applied a Gaussian
198 filter (*sigma*=2) to the images, normalised them to their 1st and 99.9^{th} percentile, and derived the
199 sample intensities using the assumption that the 10% brightest pixels in the image represented the
200 sample. For the cell images of the antibody AC-15 and the phalloidin stain, the mean Michelson
201 contrast values of 0.44±0.08 and 0.96±0.04, as well as mean RMS contrast values of 0.15±0.03 and
202 0.19±0.01 were calculated. Consequently, images of AC-15 were used as training input and images of
203 the phalloidin stain as benchmark for L2L training. For N2N, two noise realisations of AC-15 were used
204 as training data which were acquired through sequential imaging.

205 **Figure 1B** shows the restoration of an image of AC-15 in a HeLa cell (see **Figure 1A** (*left*)) by a CNN
206 after L2L training with a 3-scale structural similarity loss function ($L_{3S\text{-}SSIM}$) (see 'Methods: Training the
207 CNN'). The CNN reduces cytoplasmic signal throughout the cell body, while the relative signal of
208 filamentous actin labelled with AC-15 is increased in the restored image. In **Figure 1C**, for two regions
209 of interest (ROIs), the original cell image of AC-15 as well as the predicted images of a CNN after N2N
210 and L2L training with a L_1 and $L_{3S\text{-}SSIM}$, respectively, are shown. While noise is reduced in the restored
211 images after N2N training, resulting in an optically similar result to a 20-frame average, the relative
212 contrast between the actin filaments and the background signal that originates from depolymerised
213 protein is not enhanced. In the L2L results, however, not only image noise is removed, but also the
214 contrast of filamentous signal is clearly enhanced, even compared to the training benchmark
215 (phalloidin) (see **Figure 1D** (*left*)). Here, high intensity punctate regions originating from unspecific
216 binding or depolymerised actin are selectively filtered out by the CNN as evident in the RMS maps
217 between the raw images of AC-15 and the L2L results (see **Figure 1D** (*right*)).

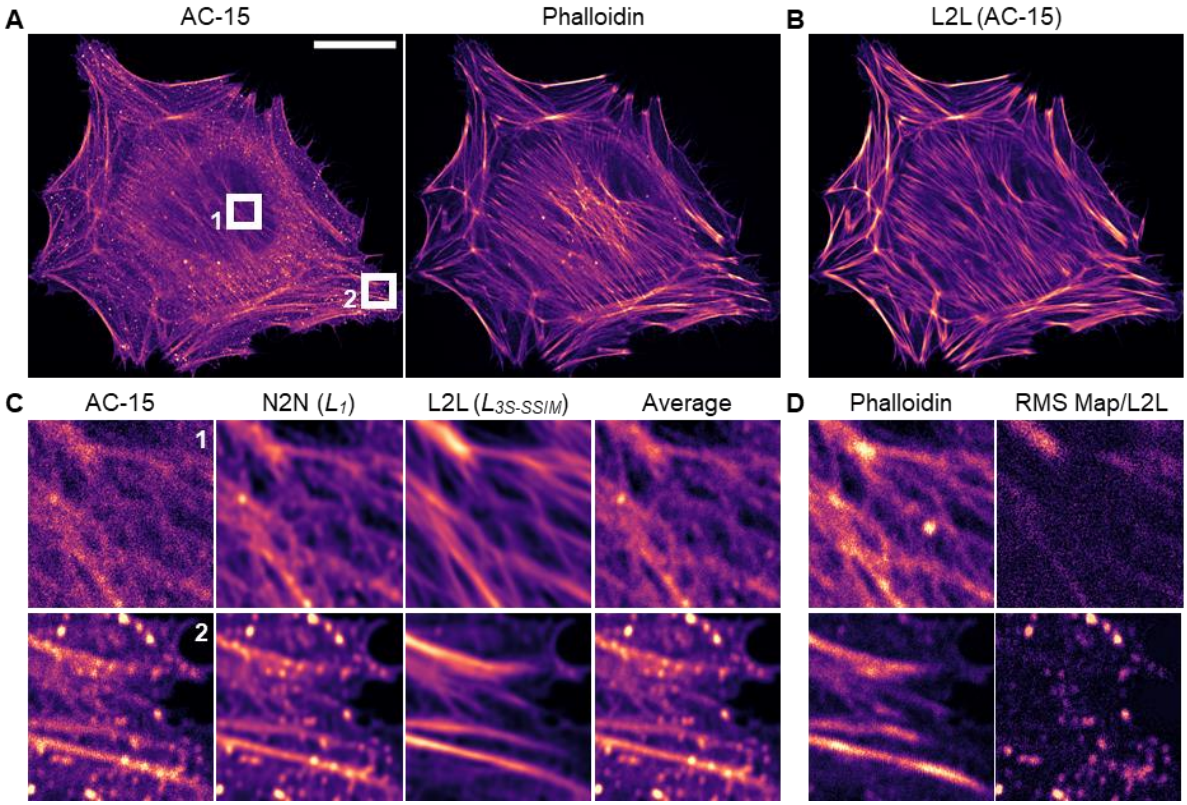

Figure 1 - Qualitative label2label (L2L) and noise2noise (N2N) results for images of actin.

(**A**) *Confocal image pair of a HeLa cell that was* fixed, permeabilized and *dual-labelled with the anti-β-actin antibody AC-15 and a phalloidin stain which was excluded from the CNN training (scale bar = 20 µm).* (**B**) *Reconstructed image of AC-15 by a CNN after L2L training with images of AC-15 and phalloidin as training input and benchmark, respectively, using a* $L_{3S\text{-}SSIM}$ *loss function.* (**C**) *Original and processed images of AC-15 for two ROIs (6 µm x 6 µm). From left to right: raw image, restored images after N2N and L2L training with a* L_1 *and* $L_{3S\text{-}SSIM}$ *loss function, respectively, and a 20-frame average.* (**D**) *The corresponding phalloidin image and the RMS map between the raw and the predicted image of AC-15 of the network after L2L training.*

In **Supplementary Information (SI) Figure 1**, the qualitative results for N2N and L2L are shown for AC-15 after training with different loss functions (L_1, $L_{5S\text{-}SSIM}$, $L_{3S\text{-}SSIM}$, L_{SSIM}), including the corresponding images of the training benchmark (phalloidin) for L2L training (see panel C) and 20-frame average images of both labels (see panel A+C) to better assess the results. For both methods, using a least absolute deviation loss function (L_1) for the training leads in comparison to more conservative predictions, where, in L2L, non-filamentous signal is filtered out by the network, but actin filaments appear relatively blurry. On the other hand, structures in restored images after training the CNN with a single-scale SSIM loss function (L_{SSIM}) appear sharp with a higher likelihood of appearing erroneous predictions. These hallucination effects are to a greater extent noticeable in the results for N2N compared to L2L. Here, punctuate regions in the images of AC-15 appear sharp in the restorations. Also, using a L_{SSIM}, filaments that appear with low contrast in the raw images of AC-15 are restored with intensity fluctuations along the structure after N2N training, which is not observed for L2L.

A	Actin Cytoskeleton					B	Microtubule Network					C	Caveolae				
	PSNR (dB)	NRMSE	MS-SSIM *M=5*	*M=3*	*M=1*	PSNR (dB)	NRMSE	MS-SSIM *M=5*	*M=3*	*M=1*	PSNR (dB)	NRMSE	MS-SSIM *M=5*	*M=3*	*M=1*
Input	16.67	0.15	0.434	0.331	0.15	17.2	0.14	0.54	0.359	0.135	14.91	0.181	0.156	0.11	0.049
L_1	19.76	0.1068	0.635	0.531	0.314	16.88	0.146	0.415	0.271	0.103	14.79	0.184	0.136	0.114	0.052
$L_{5S\text{-}SSIM}$	**20.08**	**0.1029**	**0.673**	0.565	0.339	**18.37**	**0.123**	**0.66**	**0.475**	**0.203**	**15.26**	**0.175**	**0.216**	**0.207**	**0.131**
$L_{3S\text{-}SSIM}$	20.07	0.1031	0.672	**0.567**	**0.343**	18.23	0.125	0.652	0.469	0.2	15.19	0.176	0.2	0.196	0.129
L_{SSIM}	19.91	0.1051	0.662	0.561	0.34	18.03	0.128	0.648	0.468	0.199	14.88	0.182	0.175	0.186	0.111
D	PAXILLIN					**E**	SYTOX					CD44				
Input	18.73	0.118	0.455	0.337	0.152	15.03	0.1916	0.553	0.499	0.309	20.99	0.114	0.816	0.825	0.715
L_1	19.78	0.107	0.465	0.339	0.135	36.15	0.0193	0.943	0.932	0.898	**30.05**	**0.0338**	0.942	0.916	0.841
$L_{5S\text{-}SSIM}$	**21.27**	**0.091**	**0.605**	**0.497**	0.329	36.34	0.0193	**0.958**	0.945	0.904	27.8	0.0465	**0.95**	0.921	0.838
$L_{3S\text{-}SSIM}$	21.2	0.092	0.6	0.496	**0.33**	36.27	0.0194	0.958	**0.947**	**0.91**	28.23	0.0436	0.95	**0.924**	0.845
L_{SSIM}	21.13	0.093	0.592	0.489	0.328	**36.56**	**0.019**	0.954	0.945	0.914	28.83	0.0398	0.944	0.921	**0.849**

Table 1 – Loss function-dependent evaluation of label2label (L2L) for images of different cellular structures.
Evaluation after training a CNN with **(A)** *image pairs of HeLas that were dual-labelled with an anti-actin antibody (input) and a phalloidin stain (benchmark),* (**B**) *of MeT5As that were labelled with the anti-α-tubulin antibodies DM1A (input) and YOL1/34 (benchmark),* **(C)** *of MeT5As that were labelled with antibodies against CAVIN-1 (D1P6W) (input) and CAVEOLIN-1 (4H312) (benchmark), and* (**D**) *of MeT5A, HeLa and U2OS cells that were dual-labelled with the anti-PXN antibodies 5H11 (input) and Y113 (benchmark). In* (**E**)*, the results are shown after training a CNN to separate markers in superposed images of cells that were labelled with the nuclear marker SYTOX and an anti-CD44 antibody. Average metrics were calculated between the respective training inputs or restored images of the input, respectively, after training the network with a L_1, $L_{5S\text{-}SSIM}$, $L_{3S\text{-}SSIM}$ or L_{SSIM} loss function, and the corresponding training benchmarks, using the image patch pairs that were excluded from the training for the validation (see* ***Table 2****). Metrics for the caveolae dataset were calculated after applying a Gaussian filter (sigma=1.5) due to high image noise in the benchmark images. The best value for each column is shown in bold.*

To further evaluate the performance of the network after L2L training, the average peak signal-to-noise-ratio (*PSNR*), the normalised root-mean square error (*NRMSE*), and the average *5S-SSIM*, *3S-SSIM* and *SSIM* indices were calculated for the raw or predicted images of AC-15 and the corresponding images of phalloidin, dependent on the training loss function. These were calculated using the validation image patches that were excluded from the training data (see 'Methods: Training the CNN'). All calculated metrics indicate that the correlation between the predicted images for AC-15 after L2L training and the benchmark (phalloidin) is increased compared to the original image (see **Table 1A**). Notably, the network performance increases after replacing a standard L_1 with a MS-SSIM loss function, with the $L_{5S\text{-}SSIM}$ narrowly yielding the best *PSNR* and *NRMSE*.

Label2label to enhance the structural contrast in images of the microtubule network and caveolae

To further study how L2L training impacts the contrast of distinct cellular structures in the restorations of a trained network, fluorescence image pairs were acquired of the microtubule network that has a distinct branched, spatial distribution in cells, and caveolae that are 60-100 nm large invaginations in the plasma membrane [29], [37]. For the former, fixed MeT5A cells (*N*=51) were dual-labelled with

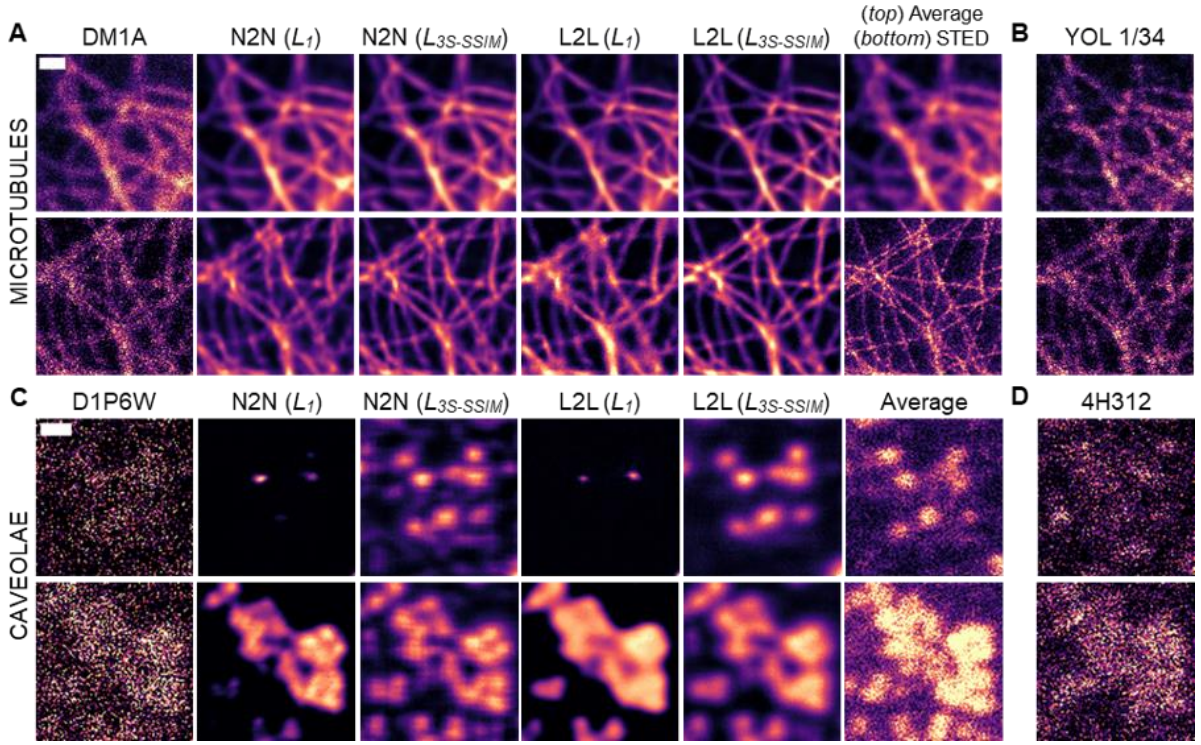

Figure 2 – Loss function-dependent label2label (L2L) and noise2noise (N2N) results for images of the microtubule network and caveolae.

Confocal images of MeT5A cells that were dual-labelled with the (**A**) *anti-tubulin antibodies DM1A and* (**B**) *YOL1/34 (scale bar = 1 µm), and STED images of MeT5A cells that were dual-labelled with* (**C**) *the anti-CAVIN-1 antibody D1P6W and* (**D**) *the anti-CAVEOLIN-1 antibody 4H312 (scale bar = 200 nm).* **(A, C)** *From left to right: raw image of a representative training input for the trainings, reconstructed images after N2N and L2L training with a* L_1 *or* $L_{3S\text{-}SSIM}$ *loss function and a corresponding 20-frame average or high resolution STED image. In* **(B, D)***, representative training benchmarks for L2L training are displayed. Shown images were excluded from the network training.*

245 two monoclonal antibodies against α-tubulin (DM1A raised in mouse and YOL1/34 raised in rat) and
246 confocal image pairs were generated. To train a CNN to increase image contrast of caveolae
247 structures, STED image pairs of caveolae (*N*=60) were acquired of fixed MeT5A cells that were dual-
248 labelled for the two essential caveolae components CAVIN-1 (D1P6W) and CAVEOLIN-1 (4H312) [28].
249 For the tubulin dataset, we calculated mean Michelson contrast values of 0.45±0.14/0.9±0.05 and
250 mean RMS contrast values of 0.13±0.03/0.17±0.02 for DM1A/YOL1/34; for the caveolae dataset, these
251 values were 0.27±0.05/0.98±0.02 and 0.13±0.02/0.22±0.02 for D1P6W/4H312 (see previous section;
252 for the caveolae dataset, the 1% brightest pixels in the image were regarded as sample). Hence, for
253 L2L training, images of DM1A and D1P6W were used as input, images of YOL1/34 and 4H312 as
254 benchmark to train a CNN as content filter for images of microtubules and caveolae, respectively.

255 In the cell images of YOL1/34 (tubulin) we observed intensity fluctuations along the microtubules that
256 might originate from selective binding to specific epitopes of polymerised tubulin or in-homogeneous
257 binding, which was not observable for the clone DM1A (see high-frame average images in **SI Figure**
258 **2C**). The microtubules appeared overall sharper in the cell images of YOL1/34 compared to DM1A,

259 with a lower, observable "haze" in the cytoplasm. This haze was likely caused by unspecific binding,
260 binding to cytosolic tubulin and/or out-of-focus signal – where the optical resolution in images of
261 DM1A labelled with the secondary antibody Alexa Fluor 633 was lower than in images of YOL1/34
262 which was conjugated to Alexa Fluor 488.

263 In **Figure 2A**, the results for the tubulin dataset after N2N and L2L training with a L_1 and $L_{3S\text{-}SSIM}$ for two
264 ROIs are displayed. The top row shows the results for a representative training image pair; in the
265 bottom, an image pair is shown that was acquired for the same sample, but with a different imaging
266 setup that allowed confocal and STED imaging (see 'Methods: Imaging'). STED images with an
267 enhanced resolution of circa a factor 3 were acquired to allow a better assessment of the restoration
268 performance of the CNN for this sample, since microtubules are insufficiently resolved in confocal
269 microscopy, especially if densely packed [37]. Structural contrast in the images of tubulin is
270 increasingly enhanced between the restorations of a network after "classical" N2N training with a L_1
271 and L2L training with a $L_{3S\text{-}SSIM}$ (see **Figure 2A**). Both methods restore images with higher contrast of
272 the microtubule structure compared to a 20-frame average image (see **Figure 2A** (*top*) and **SI Figure**
273 **2**). The restorations for the cell image of DM1A that was acquired with different imaging settings than
274 the training input exhibits a slightly less homogeneous intensity distribution along the microtubules,
275 likely due to the differing noise level (compare **Figure 2A** (*left*)). For both, N2N and L2L, the restoration
276 success is dependent on the tubule density in the image. The closer microtubules are packed in the
277 cell, the less likely is the successful recovery of separate structure by the CNN as evident by comparing
278 the restoration of the confocal image of DM1A with its STED image (see **Figure 2A** (*bottom*)). Notably,
279 the intensity fluctuations along the cellular structure in the training benchmark YOL1/34 (see **Figure**
280 **2B**) do not result in artefacts in the restored images of DM1A after L2L training. Further restorations
281 of representative training inputs are shown in **SI Figure 2** after N2N and L2L training, respectively,
282 using a L_1, $L_{5S\text{-}SSIM}$, $L_{3S\text{-}SSIM}$ or L_{SSIM}. A loss function-dependent trend for both methods is observable:
283 using a MS-SSIM loss function with decreasing scale instead of a L_1 for the training enhances the
284 contrast and sharpness of microtubules in the restorations, with L2L training leading to a higher
285 contrast of the cellular structure than N2N (see **SI Figure 2**).

286 The STED image pairs which were acquired of fixed cells that were dual-labelled for the two essential
287 caveolae proteins CAVIN-1 (D1P6W) and CAVEOLIN-1 (4H312) exhibit a low signal-to-noise ratio,
288 further amplified by the pre-processing step that was undertaken to prevent artefacts we observed
289 when training with the nearly binary, raw data (see 'Methods: Data augmentation and pre-
290 processing'; see **Figure 2C-D**). For some image pairs, we found that the correlation of the fluorescence
291 signal originating from caveolae structures was relatively low between the training input (D1P6W) and
292 benchmark (4H312) (see **SI Figure 3A+C**). This is also indicated by the calculated mean *PSNR*, *NRMSE*

293 and *MS-SSIM* indices for both images that showed the lowest correlation of the training data for all
294 datasets that were acquired for L2L training in this work (compare **Table 1A-D**). It posed the question
295 if a CNN would be prone to introduce artificial structure after L2L training with this dataset.

296 We found that the CNN performance after N2N and L2L training is highly dependent on the utilised
297 loss function (see **Figure 2C**). Using a L_1, for both training modalities, a trained CNN only restores high
298 signal-to-noise regions in the images (compare **Figure 2C** (*top*) and (*bottom*)). Using a $L_{3S\text{-}SSIM}$, however,
299 the recovery of structural signal by the CNN is much enhanced for N2N and L2L. Here, background
300 signal in the image, likely originating from unspecific labelling, is filtered-out after L2L training, while,
301 with N2N, the CNN recovers weak structure-like signal in such image areas (**Figure 2C** (*top*)). Also,
302 weak stripe-like artefacts appear in the N2N results (see also **SI Figure 3B**). These might originate from
303 small non-dynamic image corruptions from the imaging setup that are present in sequential images
304 of D1P6W, and that are picked up by a loss function that is sensitive to structural similarity of images
305 ($L_{MS\text{-}SSIM}$). The sample differences in the training data for L2L cause the CNN to restore caveolae
306 structures with slightly lower sharpness compared to N2N but it does not lead to observable
307 hallucinations effects. Notably, the level of sharpness as observed in the N2N result is not verifiable in
308 the 20-frame average image (see **Figure 2C** (*bottom*)). The introduction of artefacts by a CNN after
309 N2N training with a MS-SSIM loss function is also clearly visible in **SI Figure 3**, where restored images
310 are shown after training a CNN for N2N and L2L with a L_1, $L_{5S\text{-}SSIM}$, $L_{3S\text{-}SSIM}$ or L_{SSIM}. While low signal-to-
311 noise regions in the image are barely restored by the CNN using a L_1, using a MS-SSIM loss function
312 for N2N training, the network learns to restore background signal from the sample as caveolae-like
313 structure. This is not observed for L2L. Here, using, for example, a $L_{3S\text{-}SSIM}$ for the training, the network
314 restores the noisy image by selectively recovering caveolae structure and filtering out background
315 signal that stems from the sample, resulting in much enhanced results - also compared to the 20-
316 frame average images of both labels (see **Figure 2** and **SI Figure 3**).

317 Again, the network performance was evaluated after L2L training with different loss functions by
318 calculating the PSNR, NRMSE and different MS-SSIM indices (see **Table 1B-C**). For both datasets, the
319 calculated metrics indicate that the correlation between reconstructed and benchmark image is
320 highest after training with a $L_{5S\text{-}SSIM}$. For the tubulin dataset, a decrease in the correlation between the
321 restored image of DM1A and the benchmark (YOL1/34) after training with a L_1 is observed.

322 Training networks to reduce cytosolic content in images of PAXILLIN with paired and unpaired 323 images

324 We also trained a CNN with image pairs of two non-identical labels against the focal adhesion (FA)
325 protein PAXILLIN (PXN) [31], with the aim to reduce fluorescence signal in the images that stems from

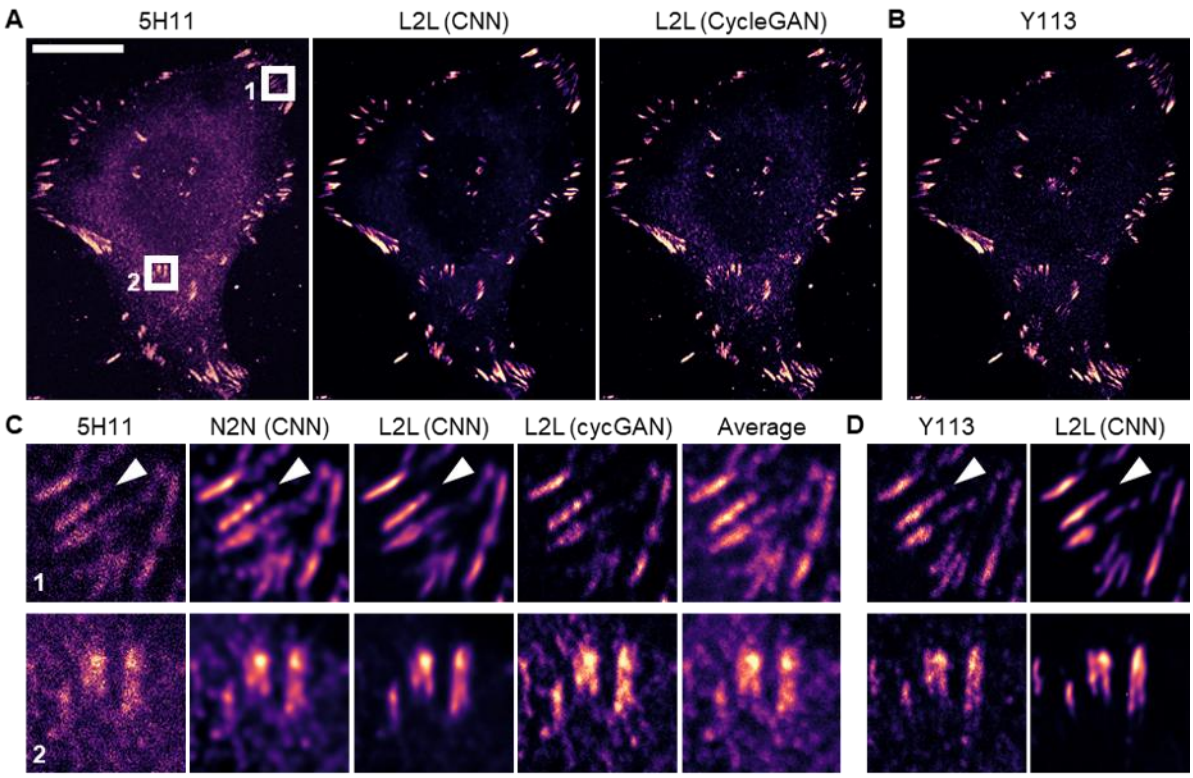

Figure 3 – Network architecture-dependent label2label (L2L) results for images of *PAXILLIN*.
Confocal images of a HeLa cell that was dual-labelled with the two anti-PAXILLIN antibodies 5H11 and Y113 which were used as training input and benchmark for L2L training. **(A)** *From left to right: raw image of 5H11, the restored images of a CNN after L2L training with paired images and of a cycleGAN that was trained with unpaired images, and* **(B)** *the corresponding image of Y113 (scale bar = 20 µm).* **(C)** *Predicted images for two ROIs (6 µm x 6 µm). From left to right: input (5H11), the restored images of a CNN after N2N and L2L training with a L_1, the restored image of a cycleGAN, and a 20-frame average.* **(D)** *Corresponding benchmark images (Y113) for L2L training and its prediction by a CNN after L2L training as outlined above. A network that was trained with L2L data in-paints focal adhesions (see white arrows) and filters out cytosolic protein (see bottom ROI) for both, the training input and benchmark. Shown images were excluded from the network training.*

326 cytosolic protein. Image pairs of fixed MeT5A (*N*=47), HeLa (*N*=17) and U2OS (*N*=13) cells were
327 acquired that were dual-labelled with the monoclonal anti-PXN antibodies 5H11 and Y113. As
328 expected, the raw IF images of both antibodies show correlating FA structures in the cells, but also a
329 diffuse signal throughout the cell body that differs in relative intensity to the FA signal between the
330 two labels (compare **Figure 3A** (*left*) and **Figure 3B**). For all cell lines we observed the same trend; the
331 images of the antibody Y113 exhibit a higher FA-to-cytosolic signal ratio compared to 5H11. To
332 determine if the cytoplasmic signal originates from clone-dependent binding to protein in the cytosol
333 or unspecific binding, shRNA mediated *PXN* knockdown MeT5A cells were generated (see 'Methods:
334 Generation and verification of knock down PAXILLIN MeT5A cells'). The knockdown was confirmed via
335 a qPCR analysis that shows a knockdown efficiency of >70% on mRNA level, and substantially lower
336 protein levels were confirmed by Western blotting (see **SI Figure 4A-B**). For both antibodies, the IF
337 signal of PXN was overall reduced in images of fixed shPXN cells in the FAs and in the cytoplasm (see

338 **SI Figure 4C**). Hence, the cytoplasmic signal that is observed in cell images of both clones is largely not
339 caused by unspecific binding. Instead, the different relative cytosolic content in cell images of 5H11
340 and Y113 indicates a differing accessibility of the respective binding sites for both clones for protein
341 that is cytosolic or bound to FAs, and that cytosolic PXN likely functions as a readily available
342 replenishable buffer for FA localised PXN.

343 All cell lines were prepared and imaged under the same conditions, and were used indistinguishable
344 to generate the training data (see 'Methods: Training the CNN'). For the cell images of 5H11/Y113
345 (N=77), mean Michelson contrast values of 0.57±0.07/0.99±0.01, and mean RMS contrast values of
346 0.15±0.01/0.18±0.02 were calculated. Consequently, cell images of 5H11 were used as training input
347 and images of Y113 as benchmark to train a network to decrease cytosolic signal in images of focal
348 adhesions. To test if an artificial network can also be trained as content filter with unpaired L2L data,
349 a cycleGAN was trained and its performance was compared to results obtained after training the CNN
350 (see 'Methods: Training a CycleGAN').

351 In **Figure 3A**, the predicted images of a CNN (using a L_1) and a CycleGAN for a cell image of 5H11 are
352 shown after L2L training with aligned and unaligned images, respectively. Both networks learn to
353 reduce cytosolic content in images of 5H11 and selectively recover FA structure, but the CNN
354 outperforms the CycleGAN for this task. While the trained cycleGAN acts as content filter of cytosolic
355 signal, high intensity areas in the cell cytoplasm that do not stem from FAs are, in part, still present in
356 the predicted images with a tendency to translate intensity fluctuations in the input as weak structure
357 (**Figure 3C** (*bottom*)). A similar effect is observed after training a CNN for N2N, using a MS-SSIM loss
358 function (see **SI Figure 5B**). Here, the CNN learns to artificially accentuate intensity fluctuations in the
359 cytosol in restored images which become more pronounced with a decreasing number of iterations
360 (M), leading to very different qualitative N2N results after using a L_1 and a L_{SSIM}. These artefacts are
361 much less pronounced in the L2L results (see **SI Figure 5B**). However, contrary to the results of the
362 evaluation (see **Table 1D**) that, again, indicate the highest network performance after using a $L_{5S\text{-}SSIM}$,
363 subjectively, the L_1 loss function was best suited to train a CNN as filter for cytosolic signal for this
364 dataset.

365 After L2L training with a L_1, cytosolic signal is clearly reduced in the predicted images compared to the
366 high average image or N2N result, resulting in images with increased contrast of the FAs (see **Figure**
367 **3C**). In addition, the trained CNN in-paints focal adhesion structures that are inhomogeneously
368 labelled (see white arrows in **Figure 3C**). Also, we found that the CNN restored images of cells labelled
369 with Y113 with decreased cytosolic content as well, although these images were used as benchmark,
370 not input for the training (see **Figure 3D**).

Training a CNN to separate cellular structures in superposed images

Lastly, the ability of a CNN to filter-out features in fluorescence images based on their spatial intensity distribution was tested by training a network to separate superposed confocal images of two different cellular targets. For that, fixed MeT5A cells were stained with the nuclear marker SYTOX Green and labelled with an antibody against CD44, a plasma membrane protein. Then, image pairs (*N*=58) were acquired of both markers (superposed) and of each marker seperately (see 'Methods: Imaging'). The spatial distribution in the cell of both targets partly overlapped in the images, but the targets were structurally distinguishable - with the nucleus appearing with high intensity in the cell centre and CD44 distributed at the periphery of the cell (see **Figure 4A**). The CNN was trained with the superposed image of both structures as training input in a two channel image, and the separate cell images of SYTOX and CD44, respectively, as training benchmark (see 'Methods: Training the CNN'). The qualitative results in **Figure 4** for an example image pair show that a CNN seperates the nucleus and plasma membrane marker in the input image successfully after the training. Noticably, similar to N2N, image jitter and noise that are present in the input image are removed by the network in the restorations (see **Figure 4B**). However, the CNN slightly blurs structure in the restorations and overlapping structures in the nuclear area are mostly but not fully recovered in the images of CD44. A loss function-dependent evaluation of the network performance showed no clear trend as to which loss function was best suited to train the CNN as separator of the two structures (see **Table 1E**).

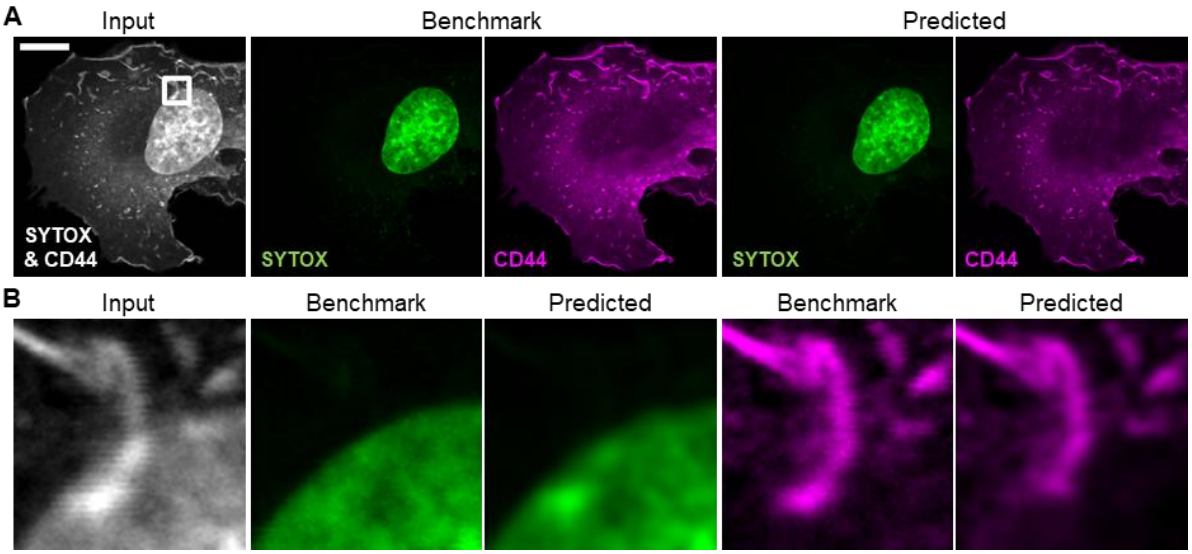

Figure 4 – Qualitative results after training a CNN to separate cellular structures in superposed images of a nuclear stain and an antibody against a plasma membrane protein.

(**A**) *Training input and benchmark images of a MeT5A cell that was dual-labelled with the nuclear stain SYTOX Green and an anti-CD44 antibody, and corresponding reconstructions after training a CNN with a* $L_{3S\text{-}SSIM}$ *(scale bar = 10 µm). The images for training the CNN were obtained via sequential imaging, using different excitation wavelengths.* (**B**) *Qualitative result for a ROI (5 µm x 5 µm). Prediction success is dependent on the level of superposition of both labels. Structures appear slightly blurry in the restorations compared to the benchmark, but image noise and jitter are reduced. The shown images were excluded from the training.*

Testing the robustness of label2label

The robustness of L2L training was evaluated for the actin (N_{tot}=68), tubulin (N_{tot}=51), caveolae (N_{tot}=60) and PAXILLIN (N_{tot}=77) dataset by studying how much the network performance is impacted by specific image pairs that are used to generate the training data. For that, repeated cross-validations were conducted with randomly selected image pairs *N* from the total dataset (N_{tot}). For the actin and PAXILLIN dataset, we conducted 8-fold cross-validations with *N* = 8, 16, 32 and 64; for the tubulin and caveolae dataset, we conducted 10-fold cross-validations with *N* = 10, 30 and 50. We increased the number of repetitions for small *N*, and the epoch number for the training was linearly adapted to *N* to prevent overfitting (see 'Methods: Training the CNN', **Table 3**). The difference between this approach and the default validation in the CSBDeep framework is that in the latter the validation is conducted via a train/test split of the training data which is generated from all raw image pairs. This way, image patches generated from a specific image pair appear in both, the test (validation) and the training data, making it impossible to assess how much the network performance depends on if a specific image pair is used for the training.

The mean relative change of the *NRMSE* and *5S-SSIM* index between the input and the restored image (both versus the reference (=training benchmark)) are shown in **Figure 5**. Each data point represents the mean value of a cross-validation dependent on *N*. A Gaussian filter (*sigma*=1.5) was applied to images of caveolae prior to the calculations since noise levels were so high in the raw input images that no trend was observable for unprocessed data. The results for nearly all datasets show a similar

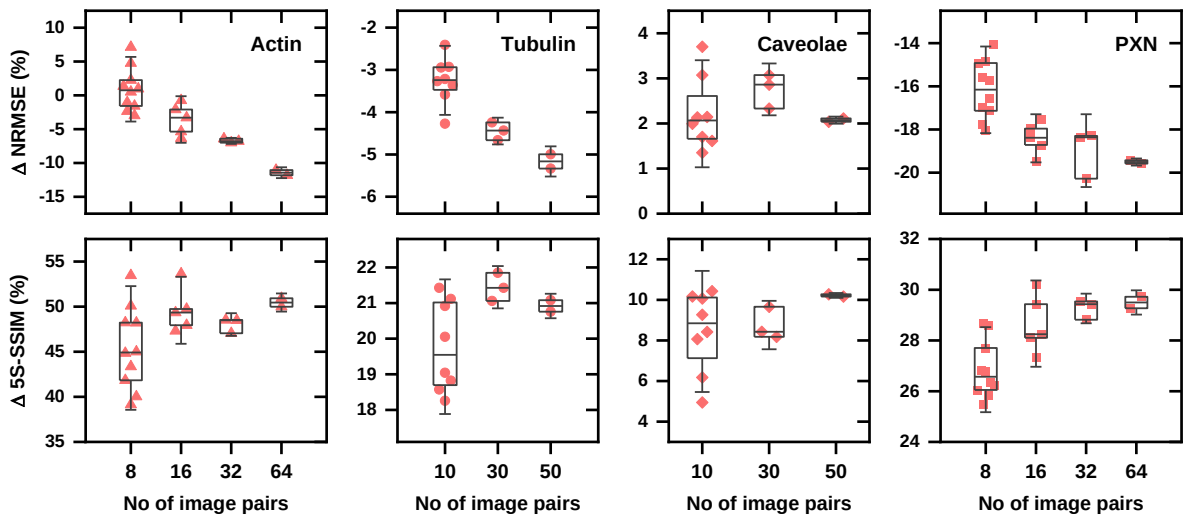

Figure 5 - Repeated cross-validation for L2L training.

The mean relative change between the initial (input and benchmark) and final (restoration and benchmark) NRMSE and 5-scale SSIM index after L2L training with image pairs of cells that were dual-labelled for the actin cytoskeleton (N=68), tubulin (N=51), caveolae (N=60) or PAXILLIN (N=77), dependent on the number of raw image pairs that were randomly selected from the total dataset for the cross validation. Each data point is the mean value for an 8-fold (actin, PAXILLIN) or 10-fold (tubulin, caveolae) cross-validation that was repeated for small image pair numbers.

408 trend: even when using a small *N*, the structural similarity to the benchmark increases for restored
409 images compared to the input. However, the calculated *ΔNRMSE* and *Δ5S-SSIM* indices are dependent
410 on the particular images that are used for the training – indicated by a wide distribution for small *N*.
411 This could indicate that certain acquired image data is better suited to train the network, or easier to
412 predict for the network. As expected, on average, the highest performance was achieved using a high
413 *N*. While the results for *Δ5S-SSIM* for all datasets indicate that with $N > 30$ or 32, respectively, the
414 network performance is relatively consistent, the *ΔNRMSE* improves continuously with increasing *N*.
415 Here, the trend of *ΔNRMSE* deviates for the caveolae dataset for which only slight changes are
416 observed between different *N*, without a clear trend.

417 Discussion

418 We show that a CNN can be successfully trained to filter out unspecific, label-induced fluorescence
419 signals detected in the cell cytoplasm in IF images of cellular structures, using images of two non-
420 identical labels as training data that target the same structure but exhibit systematic image
421 differences. L2L is different to restoration methods that use images of the same label as training data,
422 for example, N2N. While after N2N training a CNN restores all signals originating from the label
423 without distinction, a CNN systematically learns to disregard non-structural signals after L2L training.
424 We found that a network trained with L2L data restored images with high contrast of the target
425 structure, even compared to the training benchmark or its high frame average image (see, for
426 example, **Figure 2A+C**). The trained network could further be utilised to improve images that were not
427 used as input for the training. For instance, while cytosolic content was present in images of cells
428 labelled with Y113 which were used as benchmark to train the network as content filter of cytosolic
429 PXN, it was nearly eradicated in the restoration by a trained CNN (see **Figure 3D**).

430 The network performance as content filter after L2L training was dependent on the level of correlation
431 between the images of the two labels and the training loss functions. Using a single-scale SSIM loss
432 function for the training increased the likelihood of hallucination effects in restored images after L2L
433 training, especially for the PXN dataset where cytosolic content in the cell body was not entirely
434 without structure and present in both, training input and output. However, a MS-SSIM loss function
435 was better suited to train a network to restore sharp cellular structures. Here, the restorations
436 increasingly (with *M*) converged to results obtained with a L_1 (see **SI Figure 1**-**3**, **5**). For images of actin,
437 tubulin and caveolae we determined that using a $L_{3S\text{-}SSIM}$ loss function led qualitatively to the best
438 results. For these datasets, the to-filter-out signal deviated sufficiently between the image pairs,
439 allowing the network to clearly distinguish to the cellular structure that correlated in the images of
440 both labels. For the PXN dataset, a L_1 was more suited to train a CNN to recover FAs only, likely due to

441 the correlating cytosolic signal in the training images, albeit both at different relative intensity to the
442 FA signal (see **Figure 3A-B**).

443 Thus far, most deep-learning based image restoration methods have relied on image pairs of the same
444 label with differing resolution or photon counts as training data. For such training data, the N2N results
445 suggest that powerful loss functions like the MS-SSIM loss function are prone to overestimate
446 structural signal, resulting in increased hallucination effects in the restorations (see, for example, N2N
447 results in **SI Figure 3B+5B**). Using a MS-SSIM loss function for N2N training led to a significantly higher
448 occurrence of artefacts compared to L2L, where cytosolic, non-structural content (as present in the
449 training input for the actin, caveolae and PXN dataset) was restored with accentuated, artificial
450 contrast. Only for the tubulin dataset, where background signals in the images of both labels were
451 very unspecific, we observed a clear improvement between the restored images after N2N training
452 with a L_1 and a $L_{3S\text{-}SSIM}$, respectively (see **Figure 2A**). The qualitative N2N results for the caveolae dataset
453 indicate that a CNN picks up structure much more efficiently in very noisy images when using a $L_{3S\text{-}SSIM}$
454 instead of a L_1 (see **Figure 2C**). However, using images of the same label, again, caused the network to
455 hallucinate and non-dynamic image corruptions that were likely caused by the imaging system
456 appeared with higher contrast (see **Figure 2C** and **SI Figure 3B**).

457 Although clean benchmark data are not required for L2L and N2N training, in images of structures that
458 are not sufficiently resolved by the imaging technique, either *a posteriori* knowledge about the
459 structure or clean reference data are required to assess the qualitative performance of a trained CNN.
460 This was especially noticeable in cell images of tubulin, where the fine microtubule network was not
461 fully resolved with confocal microscopy (see **Figure 2A-B**). This led to erroneous predictions in image
462 areas with a dense microtubule network after both, N2N and L2L training.

463 We found that metrics like the *PSNR* and *NRMSE* were inadequate to forecast which loss function
464 yielded the best restorations by a CNN after L2L training - especially given that the reference image
465 was not clean, showing the cellular structure only. For instance, the calculated metrics after L2L
466 training with different MS-SSIM loss functions barely deviated for all dataset examples while,
467 qualitatively, differences in the restorations were observed (see **Table 1A-D**). While the mean SSIM
468 indices that were calculated for the input and benchmark images indicated scarcely any correlation,
469 with values around 0.05-0.15 for all L2L datasets (see **Table 1A-D**), the initial correlation between the
470 training data was higher according to the calculated *5S-SSIM* indices (by a factor of circa 3). This
471 indicates that a high-scale SSIM index is more suited to detect correlation in fluorescence images of
472 cellular structure than metrics like the *PSNR*, *NRMSE* or *SSIM* index, likely because the images are the

473 convolved signal of a sample volume rather than the strict 2D depiction of the sample at a specific
474 section. This observation fits to the theory of the MS-SSIM index [35].

475 As expected, the evaluation of repeated 8/10-fold cross-validations (dependent on the number of raw
476 image pairs that were used to generate the training data) showed that using a high number of image
477 pairs to train the CNN as content filter is advisable (see **Figure 5**). While the mean *PSNR* and *5S-SSIM*
478 index significantly increased even after L2L training with a small number of image pairs, the results
479 were dependent on the selected image pairs. Although the evaluation would be more meaningful if
480 each cross validation had been conducted with unique image pairs instead of image pairs that were
481 randomly selected from a finite dataset, the results indicate that a network converges to the optimal
482 result of a particular dataset during training (see **Figure 5**).

483 Prior to this work, it was unclear if the difference in the training data would introduce artificial
484 structure in the predicted images of a CNN after L2L training. For instance, in the caveolae dataset,
485 the sample differences between input and output were quite significant (compare **SI Figure 3A+C**),
486 and inhomogeneous labelling of the microtubule structure by the anti-tubulin antibody YOL1/34
487 (benchmark) was not visible in the training input (DM1A) (compare **SI Figure 2A+C**). Yet, we could not
488 observe that the CNN introduced artificial structure in the restored images after L2L training. Instead,
489 the sample differences proved advantageous when training with a MS-SSIM loss function to
490 significantly decrease the introduction of artificial structure in the restorations that we observed after
491 N2N training. However, an in-painting effect was observed for L2L, primarily in restorations of AC-15
492 (actin; see **Figure 1C-D**) and of 5H11 (PXN; see **Figure 3C-D**). Consequently, L2L can be used to correct
493 images for inhomogeneous binding of a stain or antibody, but the restorations by a trained CNN
494 cannot be used to quantify the distribution of the target protein in a cell. Instead, L2L could serve as
495 image pre-processing step to extract the binary information about the location of a specific structure
496 in a cell image, for example, of the cell membrane or the nucleus. Here, the systematic recovery of
497 specific structure by the network might make L2L superior to classical image processing methods.

498 Training data for L2L can be generated with one imaging setup using two detectors simultaneously,
499 which makes the images independent of stage drift and sample dynamics, and is time-efficient.
500 Further, the use of unpaired training data was explored by training a cycleGAN with unaligned images
501 of two anti-PXN antibodies (see **Figure 3A+C**). While the restored images of a cycleGAN after L2L
502 training showed a decrease in background signal, which in the PXN dataset originated from cytosolic
503 protein, the results were not comparable to the restorations obtained after training a CNN. We found
504 that, since the generator network in the cycleGAN is trained to fool a discriminator based on a noisy

benchmark (Y113), artefacts were introduced by the cycleGAN. This might be avoidable when training with cleaner reference images in the future.

The ability of a CNN to selectively restore specific cell structures is also highlighted in this work by training a CNN to separate a nuclear marker and plasma membrane protein label in superposed IF images (see **Figure 4**). The use of CNNs as content filter in IF microscopy could increase possibilities for multiplex imaging in the future. For example, CNNs could be employed to separate two or more markers in cell images that were acquired with microscopy setups that have a limited number of excitations sources or detectors. L2L could also be applied in multiplex imaging experiments in cases where antibodies are not selected based on performance but compatibility issues between the species in which they are raised.

Moreover, L2L could be a useful post-processing step in live cell imaging, where high-performance labels are rare. For that, the image pairs for the network training can be generated post-image acquisition *in vitro*, by fixing the cells and labelling with a higher performing antibody against the particular target structure. Our results for the caveolae dataset suggest that training a CNN with L2L data might be particularly advantageous to restore very noisy images, since it allows the implementation of a MS-SSIM loss function without introducing artefacts that we otherwise observed after training with image pairs of the same label (see **Figure 2C** and **SI Figure 3B**). Here, restored images after L2L training exhibited a high structure-to-background signal, clearly outperforming the corresponding 20 frame average images that were acquired with the STED microscope.

Conclusion

We present a new deep learning-based image restoration method for images of cellular structures that utilises the varying performance of labels in immunofluorescence microscopy. We show that by training a CNN, that was developed for content-aware image restoration, with images of two non-identical labels that target the same cellular structure but exhibit systematic sample differences the network learns to selectively restore the correlating signal in the images. Like other methods, L2L relies on the convention of the network to under-estimate inherently unpredictable signal. However, with L2L, not only image noise but also label-induced fluorescence signal in the cell specimen can be corrected in the images after selecting appropriate training data. The ability to correct images for unspecific binding, inhomogeneous labelling of a structure or binding to cytosolic protein makes L2L, to our knowledge, unique in comparison to other deep learning-based image restoration methods that are currently used in cell biology.

536 # Methods

537 ## Cell culture

538 For imaging, the human mesothelial cell line MeT5A (ATCC CRL-9444), the adenocarcinoma cervical
539 cancer cell line HeLa, and the human osteosarcoma cell line U2OS were used. HeLa cells were a gift
540 from Margaret Cunningham and U2OS cells were a gift from Kathryn McIntosh (both Strathclyde
541 Institute of Pharmacy and Biomedical Sciences, Glasgow, UK). MeT5A cells were grown in RPMI-1640
542 medium (Corning), supplemented with 10% (v/v) fetal bovine serum (FBS) (Labtech), 100 µg/ml
543 penicillin-streptomycin (Gibco), 1 mM sodium pyruvate (Gibco), 2 mM L-glutamine (Gibco) and 2 mM
544 HEPES buffer solution (Gibco). HeLa and U2OS cells were grown in DMEM+GlutaMAX medium (Gibco)
545 supplemented with 10% (v/v) FBS and 100 µg/ml penicillin-streptomycin. Human embryonic kidney
546 cells HEK293T were grown in DMEM supplemented with 100 µg/ml penicillin-streptomycin and 2mM
547 L-glutamine. All cells were kept at 37°C/5% CO_2 in a humidified atmosphere.

548 ## Generation and verification of knock down *PAXILLIN* MeT5A cells

549 Knockdown of MeT5A cells was obtained by a shRNA mediated knockdown using pKLO.1-vectors
550 coding for shRNAs mediated targeting *PAXILLIN* (TRC N0000123137) or control. HEK293T cells were
551 used for virus generation, and the virus was harvested, filtered and added to polybrene treated MeT5A
552 cells. The retroviral transduction of MeT5A cells was followed by puromycin selection. Stable
553 knockdown cell lines were verified by quantitative PCR (qPCR) (mRNA abundance) and Western blots
554 (protein abundance). For western blotting, cell lysates were prepared in reducing lysis buffer, boiled
555 for ten minutes and separated on conventional homemade SDS gels and developed onto Medical Blue
556 Sensitive X-Ray Film (Scientific Laboratory Supplies). The PAXILLIN specific antibody Y113 was used
557 (rabbit; ab32084, Abcam). Ponceau staining of the PVDF membrane was carried out to establish equal
558 loading. For quantitative PCR (RT-qPCR), mRNA was extracted from cells using the RNeasy plus mini
559 kit (QIAGEN). Complementary DNA (cDNA) was generated using the High-Capacity cDNA Reverse
560 Transcriptase kit (Applied Biosystems). qPCR was performed on 1 ng of cDNA using the Brilliant III
561 Ultra-Fast SYBR Green QPCR Master Mix (Agilent Technologies) and the Applied Biosystems
562 QuantStudio 5 Real-Time PCR Systems. Expression of *PAXILLIN* was analysed and normalized to
563 Hypoxanthine-guanine phosphoribosyltransferase (*HPRT1*) levels. qPCR data originate from five
564 independent biological replicates, plotted in Prism (GraphPad) and analysed using Mann-Whitney.

565 ## Sample preparation for immunofluorescence microscopy

566 If not stated otherwise, cells were plated onto #1.5 coverslips a day prior to fixation, then fixed with
567 4% paraformaldehyde for 15 min at 37°C, followed by a permeabilisation step with 2.5% FBS and 0.3%

568 TX 100 in PBS for 30 min at room temperature [38]. HeLa cells that were labelled for actin were fixed
569 6 h after plating. The following antibodies or stains were used to generate cell specimen dual-labelled
570 for the same target structure: to visualise the actin cytoskeleton in MeT5As the monoclonal anti-β-
571 actin antibody AC-15 conjugated to Alexa Fluor 488 (1:250; mouse; ab6277, Abcam) and the
572 phalloidin-Atto 565 stain (1:100; 94072, Sigma Aldrich); for α-tubulin labelling in MeT5As the two
573 monoclonal antibodies YOL1/34 conjugated to Alexa Fluor 488 (1:500; rat; ab195883, Abcam) and
574 DM1A (1:250; mouse; T6199, Sigma Aldrich); to label caveolae in MeT5As the monoclonal antibodies
575 4H312 (CAVEOLIN-1) (1:200; mouse; sc-70516, SCBT) and D1P6W (CAVIN-1) (1:200; rabbit; 69036, Cell
576 Signal. Techn.); and for PAXILLIN labelling in MeT5A, U2OS and HeLa cells the monoclonal antibodies
577 Y113 (1:250; rabbit; ab32084, Abcam) and 5H11 (1:500; mouse; MA5-13356, Life Technologies).
578 Further, fixed MeT5A cells were labelled with a nuclear SYTOX Green marker (S7020, Life
579 Technologies) and a monoclonal anti-CD44 antibody (1:100; rat; MA4400, Life Technologies). The
580 following secondary antibodies were used: anti-rabbit Alexa Fluor 488 (1:200; donkey; A-21206, Life
581 Technologies) to conjugate Y113; anti-rat Alexa Fluor 555 (1:100; goat; A-21434, Life Technologies) to
582 conjugate the antibody against CD44; anti-mouse Alexa Fluor 594 (1:200; goat; A32742, Life
583 Technologies) to conjugate 4H312; anti-mouse Alexa Fluor 633 (1:200; goat; A-11001, Life
584 Technologies) to conjugate DM1A and 5H11; and anti-rabbit Atto 647N (1:200; goat; 40839, Sigma-
585 Aldrich) to conjugate D1P6W. All IF samples were mounted in ProLong Glass Antifade Mountant (Life
586 Technologies) onto microscope slides.

587 ## Imaging

588 **Confocal Microscopy**

589 Image pairs of the IF sample labelled for the actin cytoskeleton, tubulin, PXN, as well as SYTOX Green
590 and CD44 were taken with a commercial confocal laser scanning microscope (Leica TCS SP8, Leica
591 Microsystems), using a HC PL Apo 63x/1.4 N.A. CS2 objective with no digital zoom (for image sizes see
592 **Table 2**). To acquire data for L2L training, both markers in the individual sample were imaged
593 simultaneously using the two in-built photomultiplier detectors, each equipped with a prism-based
594 tunable spectral filter. Each field of view was imaged twice to acquire the two noise realisations of the
595 sample that were used for N2N training of a CNN. The sample dual-labelled for actin was excited with
596 a 488 nm and 552 nm laser line and the two spectral detectors were set to detect light between 495-
597 540 and 560-700 nm. The samples dual-labelled for tubulin and PXN were excited with a 488 nm and
598 638 nm laser line and the two spectral detectors were set to detect light between 495-620 nm and
599 645-750 nm. The IF sample labelled for SYTOX Green and CD44 was imaged by setting the spectral
600 range of the detector to 560-660 nm. Separate images of SYTOX and CD44 were acquired exciting the

601 sample with a 488 and 552 nm laser line, respectively. A corresponding, superposed image of both
602 markers was acquired by exciting the sample with both lasers simultaneously.

603 **Stimulated emission depletion microscopy**

604 Fixed MeT5A cells dual-labelled for tubulin were further imaged with a Leica SP8 TCS 3X STED
605 microscope, using a Leica HC PL APO 100x/1.40 Oil STED WHITE objective (Leica 15506378). The
606 sample was excited with a Supercontinuum White Light Laser at 488 nm and 633 nm for confocal and
607 at 633 nm for STED imaging. For confocal imaging, two Leica PMT detectors were set to detect light
608 between 498-600 nm and 643-743 nm. For STED imaging, a Leica HyD hybrid detector was set to
609 detect light between 643-743nm. STED depletion was performed with a Leica 775 nm depletion laser
610 set to 50% with time gating from 0.3-8 ns. Pairs of confocal and STED images were acquired with a 15
611 nm pixel size. Sequential STED image pairs of the cell specimen labelled for caveolae were acquired
612 by first exciting the sample at 646 nm and detecting light between 656-750 nm, then exciting at 591
613 nm and using a spectral range of 601-650 nm for the detection. The depletion laser power was set to
614 100% with time gating from 0.3-8 ns, and the pixel size was set to 10 nm.

615 Image drift correction

616 Fluorescence images that were taken sequentially were corrected for stage drift by estimating the
617 extent of the displacement between the images. 100 image pairs of size 60 pixels x 60 pixels were
618 generated for each image in a temporal image stack, after applying a Gaussian filter (*sigma*=2) and
619 using the first detected image as benchmark. For that, the *create_patches* function from the CSBDeep
620 framework was used that cuts random image patch pairs in non-background areas of the image. For
621 each created image patch, the SSIM index (filter size=11, *sigma*=1.5) was calculated by shuffling the
622 uncorrected image patch relative to the benchmark patch by 5 pixels into all directions, effectively
623 cutting both into 50 px x 50 px patches. The shuffling vector that, on average, yielded the highest
624 structural similarity between both images was selected as optimal position for the sequential image,
625 and the images were cropped accordingly.

626 Data augmentation and pre-processing

627 Images were augmented to create more training data. For that, the images were interpolated, using
628 the zooming factors 0.5, 0.75, 1.25 and 1.5 (0.8, 0.9, 1.1 and 1.2 for the caveolae dataset), and then
629 randomly rotated by 0°, 90°, 180° or 270°. STED images for the caveolae dataset were pre-processed
630 by adding Poisson noise to broaden the image histogram that, due to being acquired with hybrid
631 detectors, was nearly binary in the raw images, resulting in poor results for the network trainings.

Prior to the training patch generation in the CSBDeep framework, a percentile normalisation was conducted (see **Table 2**).

Training the convolutional neural network

For N2N and L2L training, the CSBDeep framework was used, which is a CNN with U-Net architecture [2] that was developed for content-aware image restoration in fluorescence microscopy [10]. The CSBDeep framework (version 0.6.0) was downloaded from github and used with its default settings unless stated otherwise (https://github.com/CSBDeep/CSBDeep).

In the CSBDeep framework, training patches were generated randomly from the raw images after pre-processing (see previous section). Half of the training patches were generated from the raw images, the other half from augmented images. Validation data was generated via a 90/10 train/test split, and the training and validation loss were monitored to rule out overfitting.

A least absolute deviation loss function (L_1) and different multi-scale SSIM loss functions were used for the trainings (L_{SSIM} (M=1), $L_{3S\text{-}SSIM}$ (M=3), $L_{5S\text{-}SSIM}$ (M=5)). For a $L_{3S\text{-}SSIM}$, the weights were set to (0.2096, 0.4659, 0.3245), for a $L_{5S\text{-}SSIM}$, the filter size for the Gaussian filter was set to 7; otherwise the suggested settings in [35] were used.

The settings that were applied for the L2L trainings are shown in **Table 2**. The same settings were used to train the network for N2N, but the training data was generated from two sequential images of the respective antibody.

Dataset	**Actin**	**Tubulin**	**Caveolae**	**PAXILLIN**	**SYTOX+CD44**
Input marker	AC-15	DM1A	D1P6W	5H11	*superposed*[±]
Benchmark marker	Phalloidin	YOL1/34	4H312	Y113	SYTOX/CD44[±]
No. of raw image pairs	68+272[†]	51+204[†]	60+240[†]	77+308[†]	58
Size of raw images	$(4096\ \text{px})^2$	$(4096\ \text{px})^2$	$(7730\ \text{px})^2$	$(4096\ \text{px})^2$	$(2608\ \text{px})^2$
Percentiles for normalisation	1/99.9	1/99.9	2/99.5	1/99.9	2/99.8
No. of validation / training patches $(128\ \text{px})^2$	13,926 / 125,338	10,445 / 94,003	18,432 / 165,888	15,770 / 141,926	11,878 / 106,906
Learning rate (LR)	2E-4	2E-4	1E-5	2E-4	2E-5
Batch size / steps per epoch / epoch no.	32 / 100 / 400	32 / 100 / 500	16 / 500 / 100	32 / 100 / 500	32 / 1000 / 250

[†] augmented images, [±] two channel images

Table 2 - Training settings.

Overview of the training data and settings in the CSBDeep framework for L2L training.

To train the CNN as separator of two cellular markers (the SYTOX Green stain and a CD44 antibody) in superposed IF images, the CSBDeep Framework was trained with two channel images, where the input

consisted of the superposed image in both channels, and the separately acquired images of SYTOX and CD44 as the output channels (see **Table 2** (*right*)).

To further evaluate L2L, repeated 8- or 10-fold cross validations were conducted on the datasets using the settings as outlined in **Table 3**. The selection of the raw image pairs from the total dataset for each cross validation and the fold allocation were conducted randomly in Python. The image pairs for each training were generated as described above, including the pre-processing, and disabling the train/test split in the CSBDeep Framework. The relative change of the *NRMSE* and *5S-SSIM* index were calculated between input/benchmark and prediction/benchmark for the test images of each fold, deriving an average for each cross-validation (see **Figure 5**).

Dataset	**Actin (N=68) / PXN (N=77)** *8-fold cross validations*				**Tub. (N=51) / Cav. (N=60)** *10-fold cross validations*		
Number of repetitions	10	5	3	2	8	3	2
Total no. of raw image pairs	8	16	32	64	10	30	50
Loss function	$L_{3S\text{-}SSIM}$ / L_1				$L_{3S\text{-}SSIM}$		
LR / batch size / steps p. epoch	5E-4 / 32 / 150				5E-4/1E-5 / 32 / 150		
Epoch no.	20	40	60	120	20	60	100

Table 3 - Settings for repeated cross validations.
Overview of the settings in the CSBDeep framework that were used for repeated 8- or 10-fold cross validations, training the network for L2L with the different datasets.

Training the cycle generative adversarial network

The implementation of a CycleGAN in Pytorch was downloaded from github and, if not stated otherwise, trained with the default parameters (https://github.com/junyanz/pytorch-CycleGAN-and-pix2pix) [13]. The CycleGAN was trained with unaligned images of the PXN dataset that were pre-processed as outlined in the previous sections (see also **Table 2**), using a Least Squares GAN (LSGAN) with a ResNet-9 generator architecture and a 70x70 PatchGAN discriminator architecture. Training was conducted with a batch size of 4, an epoch number of 4 (3 with linear decay of the learning rate) and a scaling factor of 0.0005 for the network initialization.

675 # References

676 [1] C. Belthangady and L. A. Royer, "Applications, promises, and pitfalls of deep learning for fluorescence
677 image reconstruction," *Nat. Methods*, vol. 16, no. 12, pp. 1215–1225, Dec. 2019, doi: 10.1038/s41592-
678 019-0458-z.

679 [2] O. Ronneberger, P. Fischer, and T. Brox, "U-Net: Convolutional Networks for Biomedical Image
680 Segmentation," *Med. Image Comput. Comput. Interv. – MICCAI 2015. MICCAI 2015. Lect. Notes Comput.*
681 *Sci.*, vol. 9351, pp. 234–241, 2015, doi: 10.1007/978-3-319-24574-4_28.

682 [3] C. Ounkomol, S. Seshamani, M. M. Maleckar, F. Collman, and G. R. Johnson, "Label-free prediction of
683 three-dimensional fluorescence images from transmitted-light microscopy," *Nat. Methods*, vol. 15, no.
684 11, pp. 917–920, Nov. 2018, doi: 10.1038/s41592-018-0111-2.

685 [4] E. M. Christiansen *et al.*, "In Silico Labeling: Predicting Fluorescent Labels in Unlabeled Images," *Cell*, vol.
686 173, no. 3, pp. 792–803, Apr. 2018, doi: 10.1016/J.CELL.2018.03.040.

687 [5] T. Falk *et al.*, "U-Net: deep learning for cell counting, detection, and morphometry," *Nat. Methods*, vol.
688 16, no. 1, pp. 67–70, Jan. 2019, doi: 10.1038/s41592-018-0261-2.

689 [6] J. C. Caicedo *et al.*, "Evaluation of Deep Learning Strategies for Nucleus Segmentation in Fluorescence
690 Images," *Cytom. Part A*, vol. 95, no. 9, pp. 952–965, Sep. 2019, doi: 10.1002/cyto.a.23863.

691 [7] M. C. Daniel *et al.*, "Automated segmentation of the corneal endothelium in a large set of 'real-world'
692 specular microscopy images using the U-Net architecture," *Sci. Rep.*, vol. 9, p. 4752, Dec. 2019, doi:
693 10.1038/s41598-019-41034-2.

694 [8] I. Jansen *et al.*, "Automated Detection and Grading of Non-Muscle-Invasive Urothelial Cell Carcinoma of
695 the Bladder.," *Am. J. Pathol.*, vol. 190, no. 7, pp. 1483–1490, Jul. 2020, doi:
696 10.1016/j.ajpath.2020.03.013.

697 [9] T. Suzuki, T. Matsuzaki, H. Hagiwara, T. Aoki, and K. Takata, "Recent advances in fluorescent labeling
698 techniques for fluorescence microscopy," *Acta Histochemica et Cytochemica*, vol. 40, no. 5. Japan
699 Society of Histochemistry and Cytochemistry, pp. 131–139, 2007, doi: 10.1267/ahc.07023.

700 [10] M. Weigert *et al.*, "Content-aware image restoration: pushing the limits of fluorescence microscopy,"
701 *Nat. Methods*, vol. 15, no. 12, pp. 1090–1097, Dec. 2018, doi: 10.1038/s41592-018-0216-7.

702 [11] I. J. Goodfellow *et al.*, "Generative adversarial nets," in *Advances in Neural Information Processing*
703 *Systems*, 2014, vol. 3, no. January, pp. 2672–2680, doi: 10.3156/jsoft.29.5_177_2.

704 [12] H. Wang *et al.*, "Deep learning enables cross-modality super-resolution in fluorescence microscopy,"
705 *Nat. Methods*, vol. 16, no. 1, pp. 103–110, Jan. 2019, doi: 10.1038/s41592-018-0239-0.

706 [13] J. Y. Zhu, T. Park, P. Isola, and A. A. Efros, "Unpaired Image-to-Image Translation Using Cycle-Consistent
707 Adversarial Networks," in *Proceedings of the IEEE International Conference on Computer Vision*, Dec.

2017, pp. 2242–2251, doi: 10.1109/ICCV.2017.244.

[14] L. von Chamier *et al.*, “Democratising deep learning for microscopy with ZeroCostDL4Mic,” *Nat. Commun.*, vol. 12, no. 1, p. 2276, Dec. 2021, doi: 10.1038/s41467-021-22518-0.

[15] S. Lim, S. E. Lee, S. Chang, B. Sim, and J. C. Ye, “CycleGAN with a blur kernel for deconvolution microscopy: Optimal transport geometry,” *IEEE Trans. Comput. IMAGING*, vol. 6, pp. 1127–1138, 2020.

[16] A. Krull, T.-O. Buchholz, and F. Jug, “Noise2Void - Learning Denoising from Single Noisy Images,” *Proc. IEEE Conf. Comput. Vis. Pattern Recognit.*, pp. 2129–2137, 2019, doi: 10.1109/CVPR.2019.00223.

[17] M. Prakash, A. Krull, and F. Jug, “DivNoising: Diversity Denoising with Fully Convolutional Variational Autoencoders,” *arXiv Prepr.*, 2020, Accessed: Jul. 24, 2020. [Online]. Available: http://arxiv.org/abs/2006.06072.

[18] J. Lehtinen *et al.*, “Noise2Noise: Learning Image Restoration without Clean Data,” *Proc. 35th Int. Conf. Mach. Learn.*, vol. 80, pp. 2965–2974, Jul. 2018.

[19] C. B. Saper, “A guide to the perplexed on the specificity of antibodies,” *J. Histochem. Cytochem.*, vol. 57, no. 1, pp. 1–5, 2009, doi: 10.1369/jhc.2008.952770.

[20] D. M. Miller and D. C. Shakes, “Immunofluorescence Microscopy,” *Methods Cell Biol.*, vol. 48, pp. 365–394, Jan. 1995, doi: 10.1016/S0091-679X(08)61396-5.

[21] C. Wagner *et al.*, “Dynamic force spectroscopy on the binding of monoclonal antibodies and tau peptides,” *Soft Matter*, vol. 7, no. 9, pp. 4370–4378, May 2011, doi: 10.1039/c0sm01414a.

[22] R. Dominguez and K. C. Holmes, “Actin Structure and Function,” *Annu. Rev. Biophys.*, vol. 40, no. 1, pp. 169–186, Jun. 2011, doi: 10.1146/annurev-biophys-042910-155359.

[23] P. Vedula *et al.*, “Diverse functions of homologous actin isoforms are defined by their nucleotide, rather than their amino acid sequence,” *Elife*, vol. 6, Dec. 2017, doi: 10.7554/eLife.31661.

[24] C. Suarez and D. R. Kovar, “Internetwork competition for monomers governs actin cytoskeleton organization,” *Nature Reviews Molecular Cell Biology*, vol. 17, no. 12. 2016, doi: 10.1038/nrm.2016.106.

[25] V. Dugina, I. Zwaenepoel, G. Gabbiani, S. Clément, and C. Chaponnier, “Beta and gamma-cytoplasmic actins display distinct distribution and functional diversity.,” *J. Cell Sci.*, vol. 122, pp. 2980–2988, Aug. 2009, doi: 10.1242/jcs.041970.

[26] E. Nogales, “Structural insights into microtubule function,” *Annual Review of Biochemistry*, vol. 69. pp. 277–302, Nov. 2000, doi: 10.1146/annurev.biochem.69.1.277.

[27] F. Pellegrini and D. R. Budman, “Review: Tubulin function, action of antitubulin drugs, and new drug development,” *Cancer Investigation*, vol. 23, no. 3. pp. 264–273, 2005, doi: 10.1081/CNV-200055970.

[28] C. G. Hansen and B. J. Nichols, “Exploring the caves: Cavins, caveolins and caveolae,” *Trends in Cell*

Biology, vol. 20, no. 4. Elsevier, pp. 177–186, Apr. 01, 2010, doi: 10.1016/j.tcb.2010.01.005.

[29] I. M. Khater, F. Meng, T. H. Wong, I. R. Nabi, and G. Hamarneh, "Super Resolution Network Analysis Defines the Molecular Architecture of Caveolae and Caveolin-1 Scaffolds," *Sci. Rep.*, vol. 8, no. 1, pp. 1–15, Dec. 2018, doi: 10.1038/s41598-018-27216-4.

[30] V. Rausch and C. G. Hansen, "The Hippo Pathway, YAP/TAZ, and the Plasma Membrane," *Trends in Cell Biology*, vol. 30, no. 1. Elsevier Ltd, pp. 32–48, Jan. 01, 2020, doi: 10.1016/j.tcb.2019.10.005.

[31] F. Martino, A. R. Perestrelo, V. Vinarský, S. Pagliari, and G. Forte, "Cellular mechanotransduction: From tension to function," *Frontiers in Physiology*, vol. 9. Frontiers Media S.A., p. 824, Jul. 05, 2018, doi: 10.3389/fphys.2018.00824.

[32] H. Zhao, O. Gallo, I. Frosio, and J. Kautz, "Loss Functions for Image Restoration with Neural Networks," *IEEE Trans. Comput. IMAGING*, vol. 3, no. 1, 2017.

[33] A. B. L. Larsen, S. K. Sønderby, H. Larochelle, and O. Winther, "Autoencoding beyond pixels using a learned similarity metric," *Proc. 33rd Int. Conf. Mach. Learn.*, no. 48, pp. 1558–1566, 2016.

[34] Z. Wang, A. C. Bovik, H. Rahim Sheikh, and E. P. Simoncelli, "Image Quality Assessment: From Error Visibility to Structural Similarity," *IEEE Trans. IMAGE Process.*, vol. 13, no. 4, 2004, doi: 10.1109/TIP.2003.819861.

[35] Z. Wang, E. P. Simoncelli, and A. C. Bovik, "Multi-scale structural similarity for image quality assessment," *Conf. Rec. Asilomar Conf. Signals, Syst. Comput.*, vol. 2, pp. 1398–1402, 2003, doi: 10.1109/acssc.2003.1292216.

[36] E. Peli, "Contrast in complex images," *J. Opt. Soc. Am. A*, vol. 7, no. 10, pp. 2032–2040, 1990, doi: 10.1364/josaa.7.002032.

[37] M. Bates, B. Huang, G. T. Dempsey, and X. Zhuang, "Multicolor super-resolution imaging with photo-switchable fluorescent probes," *Science*, vol. 317, no. 5845, pp. 1749–1753, Sep. 2007, doi: 10.1126/science.1146598.

[38] V. Rausch and C. G. Hansen, "Immunofluorescence Study of Endogenous YAP in Mammalian Cells," Humana Press, New York, NY, 2019, pp. 97–106.

767 ## Contributions

768 L.S.K. designed the method, prepared the samples for imaging, generated the imaging data and
769 wrote/implemented Python scripts for pre-processing, trainings and evaluations. C.G.H. and O.S.
770 developed the *PXN* knockdown cells. O.S. validated the knockdown. J.V. and L.S.K. took the confocal-
771 STED image pairs. L.S.K., C.G.H. and G.M. wrote the manuscript, with input from all authors.

772 ## Competing Interests

773 The authors have no competing interests to declare.

774 ## Acknowledgements

775 L.S.K. was supported by the Medical Research Council and Engineering and Physical Sciences Research
776 Council Centre for Doctoral Training in Optical Medical Imaging (Optima), grant number
777 EP/L016559/1. J.V. was supported by the Wellcome Trust, grant number 208345/Z/17/Z. STED imaging
778 was performed at the Edinburgh Super Resolution Imaging Consortium (ESRIC), which is supported by
779 the MRC and the Wellcome Trust. Work on-going in the Gram Hansen lab is supported by a University
780 of Edinburgh Chancellor's Fellowship, as well as by the Worldwide Cancer Research and the June
781 Hancock Mesothelioma Research Fund (JHMRF). G.M. was supported by the grants MR/K015583/1,
782 BB/P02565X/1 and BB/T011602/1. The authors thank Martin Weigert (Swiss Federal Institute of
783 Technology Lausanne, Switzerland) for his helpful feedback.

Supplementary Information

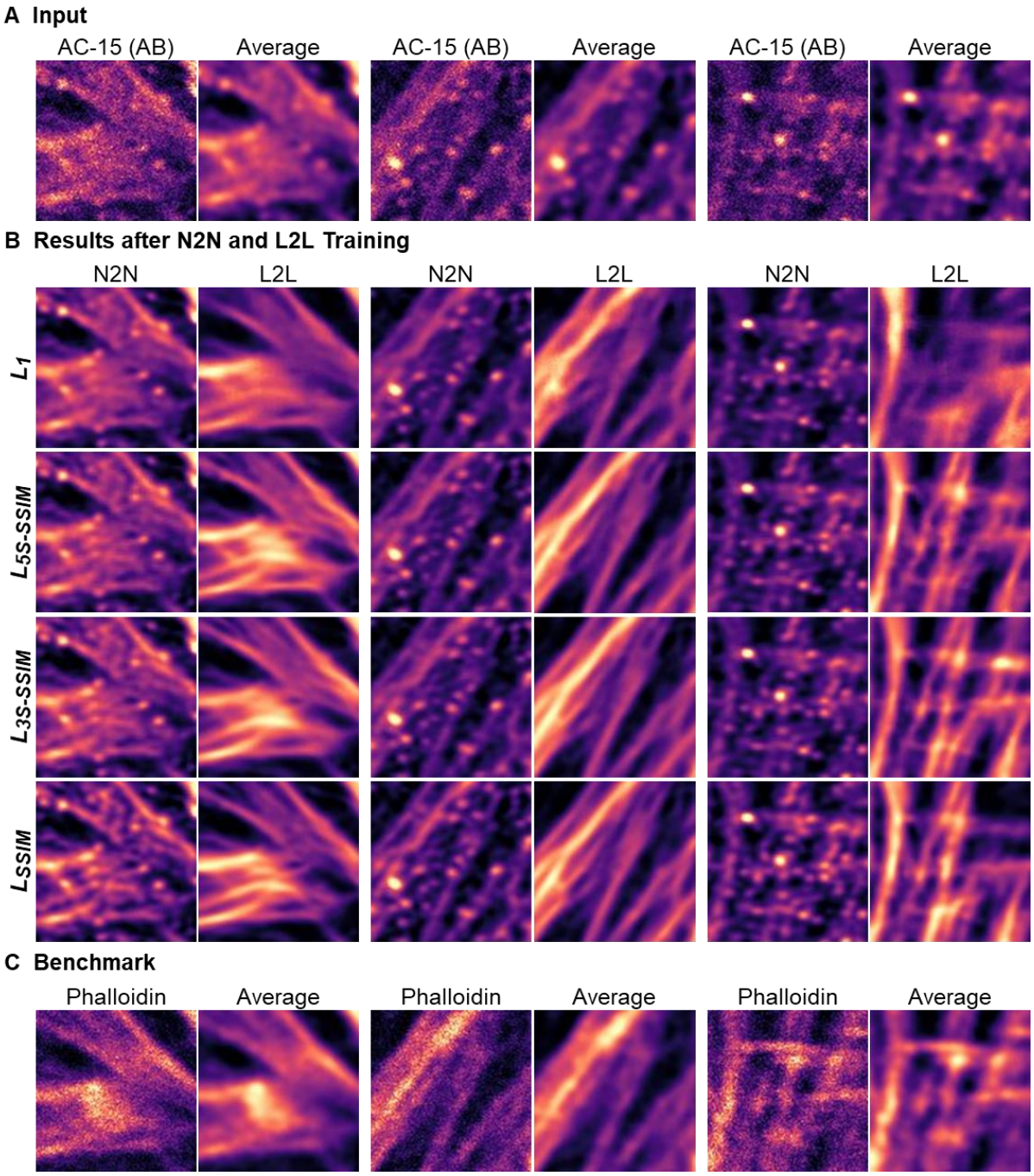

SI Figure 1 – Loss function-dependent label2label (L2L) and noise2noise (N2N) results for images of actin. Three representative examples of confocal image pairs of HeLa cells that were dual-labelled with the anti-β-actin antibody (AB) AC-15 and a phalloidin-Atto 565 stain. (**A**) Images of AC-15 in a HeLa cell and corresponding 20-frame average images. (**B**) Restored images of AC-15 by a CNN after N2N and L2L training, dependent on the training loss function. For N2N training, two sequential images of AC-15 in HeLa cells were used as training input and benchmark. For L2L training, benchmark images were replaced by (**C**) cell images of a phalloidin stain. The shown images were excluded from the trainings and contrast adjusted to the 2nd and 99.8th percentile (image dimensions: 4.5 µm x 4.5 µm).

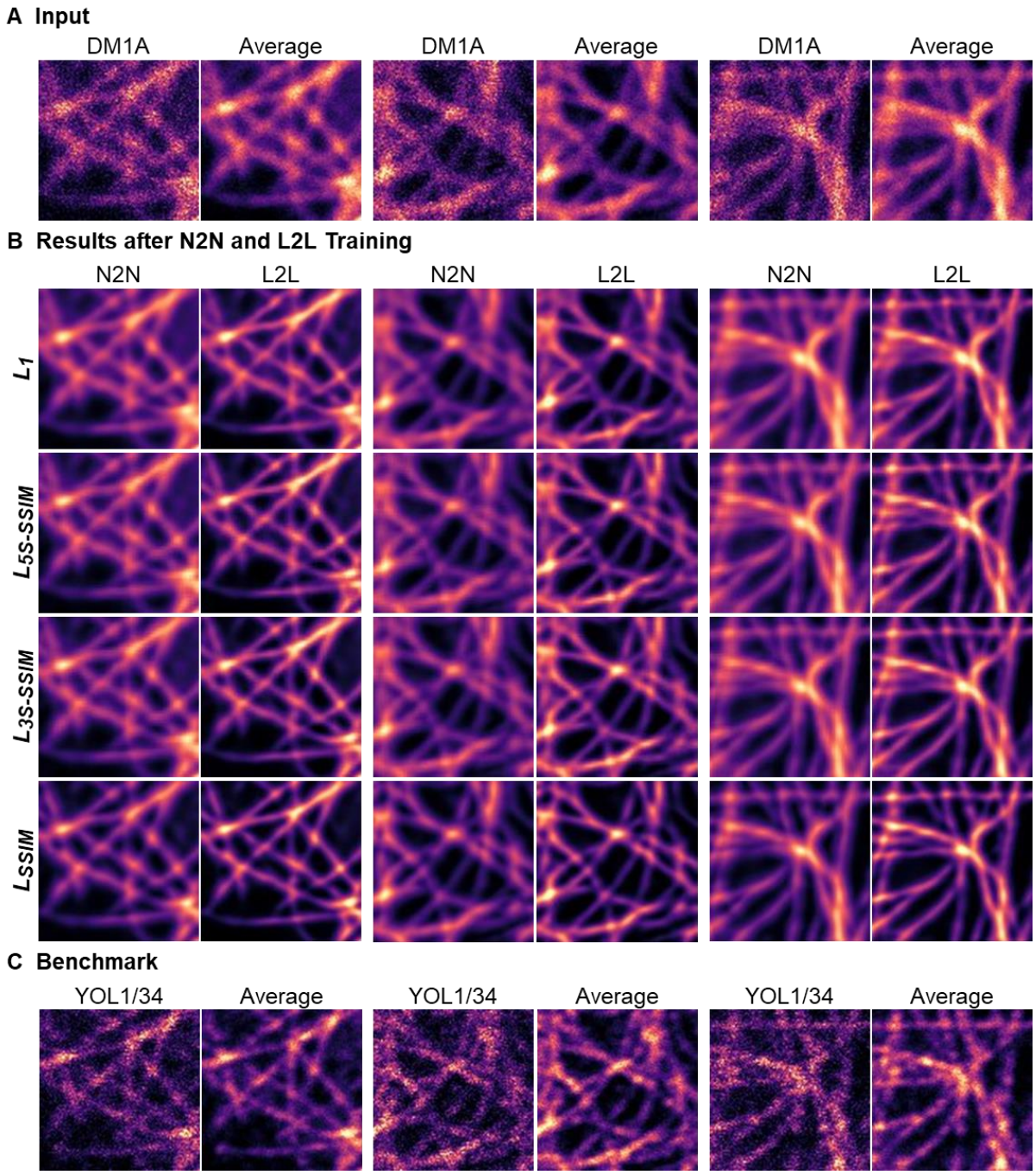

SI Figure 2 – Loss function-dependent label2label (L2L) and noise2noise (N2N) results for images of tubulin. Three representative examples of confocal image pairs of MeT5A cells that were dual-labelled with the anti-α-tubulin antibodies DM1A and YOL1/34. (**A**) Images of DM1A in MeT5A cells and corresponding 20-frame average images. (**B**) Restored images of DM1A in MeT5A cells by a CNN after N2N and L2L training, dependent on the training loss function. For N2N training, two sequential images of the DM1A signal in MeT5A cells were used as training input and benchmark. For L2L training, benchmark images were replaced by (**C**) cell images of the anti-α-tubulin antibody YOL1/34. The shown images were excluded from the trainings and contrast adjusted to the 2nd and 99.8th percentile (image dimensions: 4.5 µm x 4.5 µm).

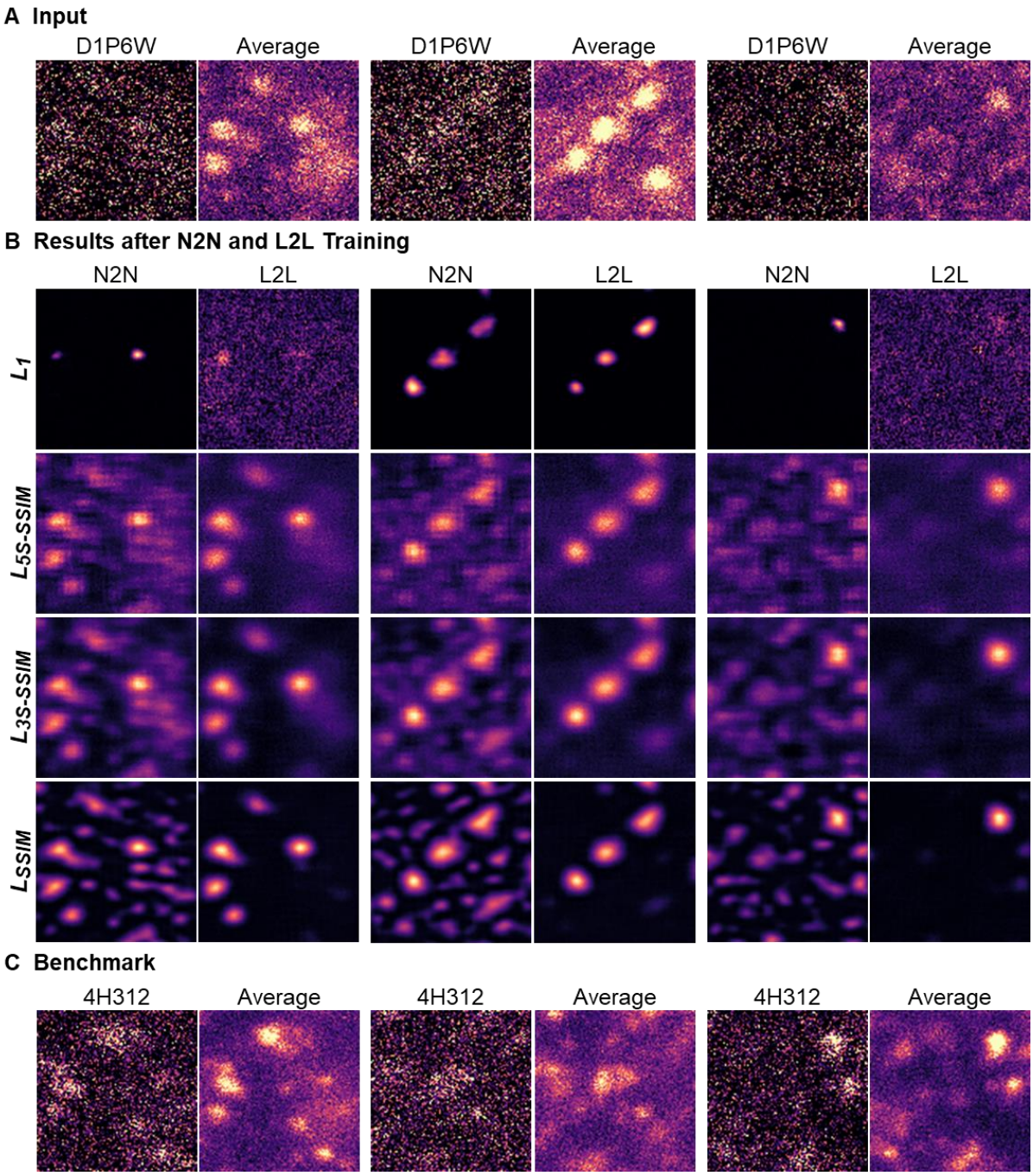

SI Figure 3 – Loss function-dependent label2label (L2L) and noise2noise (N2N) results for images of caveolae. Three representative examples of STED image pairs of MeT5A cells that were dual-labelled with the anti-CAVIN-1 antibody D1P6W and anti-CAVEOLIN-1 antibody 4H312. (**A**) Images of D1P6W in MeT5A cells and corresponding 20-frame average images. (**B**) Restored images of D1P6W in MeT5A cells by a CNN after N2N and L2L training, dependent on the training loss function. For N2N training, two sequential images of the D1P6W signal in MeT5A cells were used as training input and benchmark. For L2L training, benchmark images were replaced by (**C**) cell images of the antibody 4H312. The shown images were excluded from the trainings and contrast adjusted to the 2nd and 100th percentile (image dimensions: 1 µm x 1 µm).

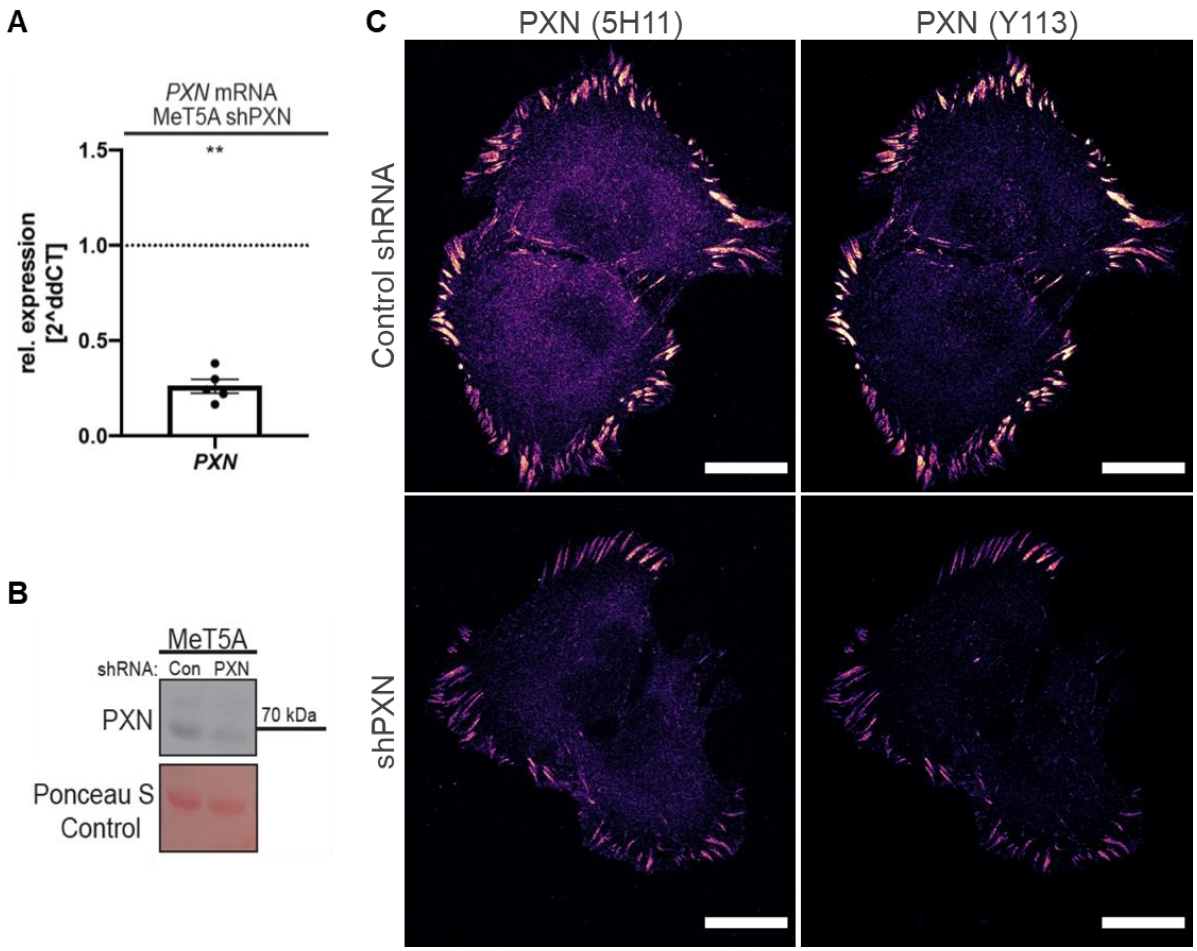

SI Figure 4 - *PAXILLIN* (*PXN*) knockdown in MeT5A cells. PXN is a focal adhesion molecule. (**A**) Results of a RT-qPCR analysis, including the standard error of the mean: the relative expression of the *PXN* knockdown cells is 26.14±0.04%. (**B**) Western analysis of cell lysates of MeT5A cells visualising the PXN protein knockdown, with Ponceau stain ensuring equal loading. The monoclonal anti-PXN antibody Y113 was used. The PXN expression is reduced by around a half in the knockdown cells compared to the control. (**C**) Immunofluorescence images of MeT5A cells that were dual-labelled with the anti-PXN antibodies (*left*) 5H11 and (*right*) Y113 after (*top*) mock-infection and (*bottom*) shRNA mediated *PXN*-knockdown. The low signal of cytosolic protein in the knockdown cells for both antibodies indicate that the difference in cytosolic signal between the two, as observed in the control cells, originates from clone-dependent antibody binding to cytosolic PXN rather than unspecific binding (scale bar = 20 µm).

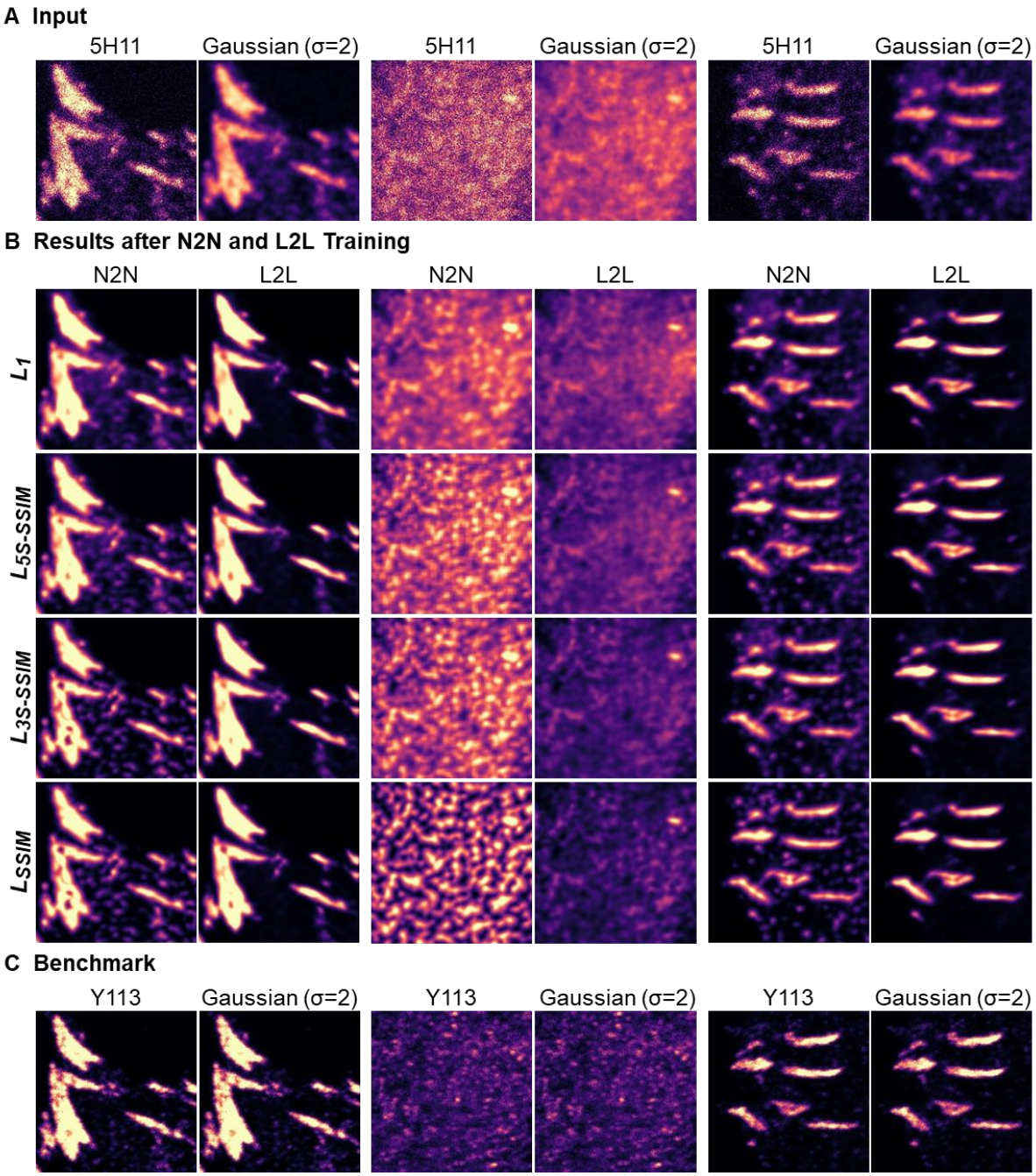

SI Figure 5 – Loss function-dependent label2label (L2L) and noise2noise (N2N) results for images of focal adhesions. Three representative examples of confocal image pairs of MeT5A cells that were dual-labelled with the anti-PAXILLIN (PXN) antibodies 5H11 and Y113. (**A**) Images of 5H11 in MeT5A cells and corresponding Gaussian filter images (σ=2). (**B**) Restored images of 5H11 in a MeT5A cell by a CNN after N2N and L2L training, dependent on the training loss function. For N2N training, two sequential images of 5H11 in MeT5A cells were used as training input and benchmark. For L2L training, benchmark images were replaced by (**C**) cell images of the anti-PXN antibody Y113. The shown images were excluded from the trainings. Images of 5H11 and Y113 were contrast adjusted to the 2nd and 99.8th percentile of the respective original image (image dimensions: 9.1 µm x 9.1 µm).